






## Article

# Relativistic Study on the Scattering of $e^{\pm}$ from Atoms and Ions of the Rn Isonuclear Series

Mahmudul H. Khandker <sup>1</sup>, A. K. Fazlul Haque <sup>1</sup>, M. M. Haque <sup>1,\*</sup>, M. Masum Billah <sup>1</sup>, Hiroshi Watabe <sup>2</sup>  
and M. Alfaz Uddin <sup>3</sup>

<sup>1</sup> Atomic and Molecular Physics Lab, Department of Physics, University of Rajshahi, Rajshahi 6205, Bangladesh; kmhasan\_phy@yahoo.com (M.H.K.); fhaque@ru.ac.bd (A.K.F.H.); masumphy@ru.ac.bd (M.M.B.)

<sup>2</sup> Cyclotron and Radioisotope Center, Division of Radiation Protection and Safety Control, Tohoku University, 6-3 Aoba, Aramaki, Aoba, Sendai 980-8578, Japan; watabe@cyric.tohoku.ac.jp

<sup>3</sup> Department of Physics, Pabna University of Science and Technology, Pabna 6600, Bangladesh; uddinmda@yahoo.com

\* Correspondence: mhpdru@gmail.com; Tel.: +880-171-634-6268

**Abstract:** Calculations are presented for differential, integrated elastic, momentum transfer, viscosity, inelastic, total cross sections and spin polarization parameters  $S$ ,  $T$  and  $U$  for electrons and positrons scattering from atoms and ions of radon isonuclear series in the energy range from 1 eV–1 MeV. In addition, we analyze systematically the details of the critical minima in the elastic differential cross sections along with the positions of the corresponding maximum polarization points in the Sherman function for the aforesaid scattering systems. Coulomb glory is investigated across the ionic series. A short range complex optical potential, comprising static, polarization and exchange (for electron projectile) potentials, is used to describe the scattering from neutral atom. This potential is supplemented by the Coulomb potential for the same purpose for a charged atom. The Dirac partial wave analysis, employing the aforesaid potential, is carried out to calculate the aforesaid scattering observables. A comparison of our results with other theoretical findings shows a reasonable agreement over the studied energy range.

**Keywords:** electron and positron scattering; spin asymmetry; critical minima; total polarization; coulomb glory



**Citation:** Khandker, M.H.; Haque, A.K.F.; Haque, M.M.; Billah, M.M.; Watabe, H.; Uddin, M.A. Relativistic Study on the Scattering of  $e^{\pm}$  from Atoms and Ions of the Rn Isonuclear Series. *Atoms* **2021**, *9*, 59. <https://doi.org/10.3390/atoms9030059>

Academic Editor: Grzegorz Piotr Karwasz

Received: 6 August 2021

Accepted: 23 August 2021

Published: 27 August 2021

**Publisher's Note:** MDPI stays neutral with regard to jurisdictional claims in published maps and institutional affiliations.



**Copyright:** © 2021 by the authors. Licensee MDPI, Basel, Switzerland. This article is an open access article distributed under the terms and conditions of the Creative Commons Attribution (CC BY) license (<https://creativecommons.org/licenses/by/4.0/>).

## 1. Introduction

Lepton scattering from atoms and ions is of immense importance in both experimental and theoretical studies. Electron ( $e^-$ ) scattering from neutral atomic targets is an efficient tool to glean projectile-target interaction [1], the structure of atoms or molecules and matter in bulk. The electrons passing through matter are not only scattered, but also produce ions of different charges. Explicit interpretation of the spectroscopic observations and theoretical modeling of the formation and time evolution of artificial, terrestrial, space and astrophysical plasmas require the electron-ion scattering cross section data [2]. On the other hand, positron-ion scattering is important for understanding the dynamics of the collisions of positrons with ions, atoms and molecules in interstellar medium [3]. For the positron ( $e^+$ ) projectile, phaseshifts are very sensitive to the polarization as the repulsive static potential partially cancels the attractive polarization potential [4]. Therefore,  $e^+$ -atom collision can furnish a useful, and sometimes more sensitive test of the techniques used for studying the lepton scattering processes.

The elastic differential cross section (DCS) data can provide detailed information on collision dynamics and the optical potential. The total cross section (TCS) as well as its integrated elastic cross section (IECS) and inelastic cross section (INCS) determine the mean free path between two elastic collisions. The momentum-transfer cross section

(MTCS) is used to compute the average momentum transferred by the projectile to the target on collision. The viscosity cross section (VCS) is needed for expansion of the multiple scattering formula used as an input to the Monte Carlo simulation of the electron transport in solids. Regarding collision dynamics, more detailed information can be unfolded by studying spin asymmetry parameters  $S$ ,  $T$  and  $U$ . The  $S$  parameter, the so called Sherman function, associated with leptons spin-polarized perpendicular to the scattering plane, serves to measure the beam polarization [5]. The angle of rotation of the component of the polarization vector in polarized projectiles can be obtained by other two parameters  $T$  and  $U$ . The determination of critical minima (CM) points in the DCS is useful as a complete spin polarization of the scattered projectile occurs in the vicinity of these CMs [6,7]. All aforesaid observables of lepton scattering from neutral atoms, ions, and molecules have many applications in various pure and applied sciences.

To date, a considerable number of attempts, both experimentally [8–11] and theoretically [12–17], have been made to study the collisions of electrons with rare-gas atoms. Due to the inertness and availability, rare-gas atoms are often used as targets in experimental studies of scattering in a goal to understand lepton-atom interaction and test collision dynamics. The recent development of rare-gas halide high-power lasers has increased interest in studies the electrons scattering from inert gases. In physical sciences radon is used as a tracer because of its short half-life (3.8 days). Despite such applications, studies on  $e^\pm$ -radon scattering, particularly across the isonuclear series, are limited. To date, as we are aware, there is no experiment on  $e^-/e^+$ -radon scattering available in the literature. The high cost and radioactivity of radon stand as barrier to a experimental research with it.

On the theoretical side, Kapil and Vats [18] performed relativistic calculations of the DCS, IECS and MTCS as well as  $S$ ,  $T$  and  $U$  for positrons scattering by radon and radium atoms in the energy range 2–500 eV. The same observables in the same energy range for electrons scattering from Yb, Rn and Ra were calculated by Neerja et al. [19]. At energies  $E_i = 20$ –1000 eV, the TCS for positron scattering from all the rare gases were reported by Baluja and Jain [12]. IECS, MTCS and VCS for the neutral atomic targets ( $Z_T = 1$ –92) were tabulated by Mayol and Salvat [20] for 100 eV to 1 GeV electrons, and by Dapor and Miotello [21] for 500–4000 eV positrons. Sin Fai Lam [13] predicted DCS, TCS and  $S$  for low energy ( $E_i \leq 30$  eV) electrons from krypton, xenon and radon atoms. It is worth mentioning that all of these cross sections were calculated only for neutral atomic targets. This fact underscores the necessity for the study of lepton-ion scattering from the perspectives of fundamental and practical importance. Furthermore, this situation motivates us to undertake the study of scatterings of electrons and positrons from radon atoms and ions up to charge state  $q^{86+}$ .

In this study, we have investigated elastic DCS, IECS, MTCS, VCS, INCS, TCS,  $S$ ,  $T$  and  $U$  for both electrons and positrons scattering from radon isonuclear series including neutral atoms as well as ions over a wider energy range of  $1 \text{ eV} \leq E_i \leq 1 \text{ MeV}$ . In DCSs of the  $e^-$ -Rn system, we have investigated CM and determined maximum spin polarization (MSP) points in the vicinity of these CMs. Coulomb glory, the amplification of elastic backscattering of electrons from positive ions owing to the electrostatic screening of nuclear potential by atomic electrons, has been investigated throughout the ionic series of radon. The aforesaid scattering observables are obtained by solving Dirac relativistic equation within the framework of partial wave analysis using a modified Coulomb potential (MCP) [15] in the form

$$V(r) = V_{\text{mc}}(r) = \frac{zqe^2}{r} + V_{\text{sr}}(r). \quad (1)$$

The first term on the right-hand side of the above equation is the long-range Coulomb potential due to the Coulomb interaction between primary electron or positron with the target with the ionic charge  $q$ .  $e$  is magnitude of the electron charge, and  $z = -1$  for

electron and +1 for positron. The short-range part,  $V_{\text{sr}}(r)$  is given by a local complex optical potential [22–25] in the form

$$V_{\text{sr}}(r) = V_{\text{op}}(r) = V_{\text{R}}(r) - iW_{\text{abs}}(r), \quad (2)$$

where,  $V_{\text{R}}(r)$  and  $iW_{\text{abs}}(r)$  denote, respectively, the real and imaginary parts of the potential. The real part consists of static, exchange and correlation–polarization potentials. The electron number density of the target, required for the generation of these components, is obtained numerically from the multiconfiguration Dirac–Fock wavefunctions [26]. In case of  $e^{\pm}$ -atom scattering, the long-range part of Equation (1) is absent and, therefore, the interaction potential becomes pure short ranged optical potential given in Equation (2). For unscreened nuclear targets, on the other hand, the short-range part of Equation (1) vanishes, and the scattering reduces to pure Coulomb scattering.

Our results are compared with other calculations available in the literature. The rest of this paper is organized as follows. Section 2 gives the outline of the theory. In Section 3, we present potential details and numerics. Results of our theory and comparison with existing calculations are given in Section 4. In Section 5, we draw our conclusions. Atomic units ( $\hbar = m_e = e = 1$ ) are used throughout unless otherwise indicated.

## 2. Theory

### 2.1. Optical Potential

In our MCP approach, the Coulomb potential is complemented by a short-range complex optical potential given in the following form

$$V_{\text{sr}}(r) = V_{\text{st}}(r) + V_{\text{ex}}(r) + V_{\text{cp}}(r) - iW_{\text{abs}}(r). \quad (3)$$

Here, the real components  $V_{\text{st}}(r)$ ,  $V_{\text{ex}}(r)$ ,  $V_{\text{cp}}(r)$  are, respectively, the static, the exchange and the correlation polarization potentials. Furthermore, the imaginary component  $W_{\text{abs}}(r)$  represents the absorption potential. The static potential  $V_{\text{st}}(r)$  arises from the electrostatic interactions of the projectile with the target electrons and protons. The exchange potential  $V_{\text{ex}}(r)$  is used to handle the non-local rearrangement collisions between primary and bound electrons arising due to their indistinguishability. For positron scattering,  $V_{\text{ex}}(r) = 0$  as there is no exchange probability between the projectile and bound electrons. The correlation polarization potential  $V_{\text{cp}}(r)$  describes the distortion of the target charge distribution by the projectile electron or positron. The absorption potential  $W_{\text{abs}}(r)$  incorporates the loss of beam intensity to various inelastic channels during the collision.

#### 2.1.1. Static Potential

The electrostatic potential  $V_{\text{st}}(r)$  in Equation (3), at a distance  $r$  from the nucleus of the target, is given by

$$V_{\text{st}}(r) = ze[\phi_n(r) + \phi_e(r)], \quad (4)$$

where,  $\phi_n(r)$  and  $\phi_e(r)$  are, respectively, potentials due to nuclear and electronic charge distributions. Under static-field approximation, the interaction potential is completely determined by the nuclear and electronic charge distributions. In the present study, we consider a Fermi nuclear charge distribution [27] and the Dirac–Fock electron density, generated from relativistic Hartree–Fock wavefunctions by Desclaux [26]. The static potential can, therefore, be presented as [28]

$$\phi_n(r) = e \int d\mathbf{r}' \frac{\rho_n(r')}{|\mathbf{r} - \mathbf{r}'|} \quad \text{and} \quad \phi_e(r) = -e \int d\mathbf{r}' \frac{\rho_e(r')}{|\mathbf{r} - \mathbf{r}'|}. \quad (5)$$

Here,  $\rho_n$  and  $\rho_e$ , the number densities of protons and orbital electrons, respectively, are normalized as

$$\int \varrho(r)4\pi r^2 dr = \begin{cases} Z - q, & \text{for } \varrho_e \\ Z, & \text{for } \varrho_n \end{cases} \tag{6}$$

with  $Z - q$  being the number of dressing electrons of the target and  $Z$ , the atomic number of the target.

### 2.1.2. Exchange Potential

The exchange potential  $V_{ex}(r)$  in Equation (3), a type of semi-classical exchange potential [29], is obtained from the non-local exchange interaction with the help of a WKB-like approximation for the wave functions. It is expressed as

$$V_{ex}(r) = \frac{1}{2}[E_i - V_{st}(r)] - \frac{1}{2}\{[E_i - V_{st}(r)]^2 + 4\pi a_0 e^4 \varrho_e(r)\}^{1/2}. \tag{7}$$

Here,  $E_i$  and  $a_0$  are the incident electron energy and the Bohr radius, respectively.

### 2.1.3. Polarization Potential

The correlation polarization potential  $V_{cp}(r)$  in Equation (3) is a combination of long range Buckingham potential  $V_{cp,B}(r)$  and a short-range correlation potential  $V_{co}(r)$ . This global type correlation-polarization potential is expressed as [30]

$$V_{cp}^{\pm}(r) \equiv \begin{cases} \max\{V_{co}^{\pm}(r), V_{cp,B}(r)\} & \text{if } r < r_c \\ V_{cp,B}(r) & \text{if } r \geq r_c, \end{cases} \tag{8}$$

where  $r_c$  is the outer radius at which the above two contributions intersect for the first time.

The long-range part, independent of the charge of the incoming projectile, has the following asymptotic form

$$V_{cp,B}(r) = -\frac{\alpha_d e^2}{2(r^2 + d^2)^2}, \tag{9}$$

with  $\alpha_d$  is the dipole polarizability of the target. The phenomenological cut off parameter  $d$  is given by [31]

$$d^4 = \frac{1}{2}\alpha_d a_0 (Z - q)^{-1/3} b_p^2, \tag{10}$$

where,  $b_p$  is an adjustable parameter that decreases as the projectile energy increases and is expressed by the following empirical formula [30]

$$b_p^2 = \max\{(E - 50 \text{ eV}) / (16 \text{ eV}), 1\}. \tag{11}$$

At  $r < r_c$ , the asymptotic expansion completely breaks down, and the interaction potential for the correlation between the projectile and electron cloud can be described by the following analytic expression given by Perdew and Zunger [32]

$$V_{co}^{(-)}(r) = -\frac{e^2}{a_0}(0.0311 \ln(r_s) - 0.0584 + 0.00133r_s \ln(r_s) - 0.0084r_s), \text{ for } r_s < 1 \tag{12}$$

and

$$V_{co}(r) = -\frac{e^2}{a_0}\beta_0 \frac{1 + (7/6)\beta_1 r_s^{1/2} + (4/3)\beta_2 r_s}{(1 + \beta_1 r_s^{1/2} + \beta_2 r_s)^2}, \text{ for } r_s \geq 1 \tag{13}$$

where,  $\beta_0 = 0.1423$ ,  $\beta_1 = 1.0529$  and  $\beta_2 = 0.3334$ .

For positron impact scattering, the present study uses the correlation potential of Jain [33] as given by

$$V_{co}^{(+)}(r) = \frac{e^2}{2a_0} \{-1.82r_s^{-1/2} + [0.051 \ln(r_s) - 0.115] \ln(r_s) + 1.167\}, \text{ for } r_s < 0.302, \tag{14}$$

$$V_{co}^{(+)}(r) = \frac{e^2}{2a_0} [-0.92305 - 0.09098r_s^{-2}], \text{ for } 0.302 \leq r_s < 0.56, \tag{15}$$

and

$$V_{co}^{(+)}(r) = \frac{e^2}{2a_0} \left[ -\frac{8.7674}{(r_s+2.5)^3} + \frac{-13.151+0.9552r_s}{(r_s+2.5)^2} + \frac{2.8655}{(r_s+2.5)} - 0.6298 \right], \text{ for } 0.56 \leq r_s < 8.0. \tag{16}$$

For  $8.0 \leq r_s \leq \infty$  (i.e., at the asymptotic region), the polarization potential is accurately given by Equation (9). The parameter  $r_s$  is given by the following equation

$$r_s \equiv \frac{1}{a_0} \left[ \frac{3}{4\pi\rho_e(r)} \right]^{\frac{1}{3}}. \tag{17}$$

#### 2.1.4. Absorption Potential

The absorption potential  $W_{abs}(r)$  in Equation (3) is a semi-relativistic imaginary potential proposed by Salvat et al. [34]. This negative imaginary term is included in the optical potential to account for the loss of incident flux from elastic channel to inelastic channels above the inelastic threshold. This absorption potential depends on the cross section for binary collisions between the projectile and target electron. Within the framework of Born-Lindhard formulation a non-relativistic formulation of the absorption potential for electron scattering can be obtained under local density approximation (LDA) as by Salvat [30]

$$W_{abs}^{nr} = A_{abs} \frac{\hbar}{2} [v_L^{nr} \rho_e(r) \sigma_{bc}(E_L, \rho_e, \Delta)]. \tag{18}$$

Here,  $v_L^{nr}$  is the non-relativistic velocity with which the projectile interacts as if it were moving within a homogeneous gas of density  $\rho_e$ . This velocity is given by

$$v_L^{nr} = \sqrt{2E_L/m_e} \tag{19}$$

corresponding to the local kinetic energy

$$E_L(r) = \begin{cases} E - V_{st}(r) - V_{ex}(r) & \text{for electron} \\ \max\{E - V_{st}(r), 0\} & \text{for positron.} \end{cases} \tag{20}$$

The term  $\sigma_{bc}(E_L, \rho_e, \Delta)$  in Equation (18) represents the non-relativistic Born approximated cross section for collisions involving energy transfer greater than a certain energy gap  $\Delta$ . This energy gap is the threshold energy for the inelastic channel and accounts for the minimum energy lost by the projectile. The energy gap adopted for the present computation is given by

$$\Delta = \begin{cases} \epsilon_1 & \text{for electron} \\ I - 6.8 & \text{for positron} \end{cases} \tag{21}$$

with  $\epsilon_1$  is the first excitation energy,  $I$  is the ionization potential and 6.8 eV is positronium binding energy.

The relativistic effects are accounted by Salvat [30] in the expression (18) by introducing the relativistic velocity

$$v_L^r = c \sqrt{\frac{E_L(E_L + 2m_e c^2)}{(E_L + m_e c^2)^2}} \tag{22}$$

The semi-relativistic form for  $W_{\text{abs}}$  is

$$W_{\text{abs}} = \frac{v_L^{\text{nr}}}{v_L} W_{\text{abs}}^{\text{nr}} = \sqrt{\frac{2(E_{rml} + m_e c^2)^2}{m_e c^2 (E_L + 2m_e c^2)}} \times A_{\text{abs}} \frac{\hbar}{2} [v_L^n \varrho_e(r) \sigma_{\text{bc}}(E_L, \varrho_e, \Delta)], \quad (23)$$

where,  $c$  is the velocity of light in vacuum. The value of the empirical parameter  $A_{\text{abs}}$  depends on the projectile-target combination and can be determined by fitting the available data. In the present calculations,  $A_{\text{abs}} = 2$  for electron and 1 for positron scattering.

### 2.2. Dirac Partial Wave Analysis

The relativistic Dirac equation for a projectile moving with a velocity  $v$  in a central field  $V_{mC}(r)$  is given as

$$[\mathbf{c}\boldsymbol{\alpha} \cdot \mathbf{p} + \beta m_0 c^2 + V_{mC}(r)] \psi(\mathbf{r}) = (E + m_0 c^2) \psi(\mathbf{r}), \quad (24)$$

with  $E + m_0 c^2$  being the total energy of the projectile and the operators  $\boldsymbol{\alpha}$  and  $\beta$ , the usual  $4 \times 4$  Dirac matrices. Solutions of the Dirac equation are the spherical waves and are given by [35]

$$\psi_{E\kappa m}(\mathbf{r}) = \frac{1}{r} \begin{pmatrix} P_{E\kappa}(r) \Omega_{\kappa, m}(\hat{\mathbf{r}}) \\ i Q_{E\kappa}(r) \Omega_{-\kappa, m}(\hat{\mathbf{r}}) \end{pmatrix}, \quad (25)$$

where  $P_{E\kappa}(r)$  and  $Q_{E\kappa}(r)$  are the upper- and lower-component radial functions and  $\Omega_{\kappa, m}(\hat{\mathbf{r}})$  are the spherical spinors.  $\kappa = (\ell - j)(2j + 1)$  is the relativistic quantum number with  $j$  and  $\ell$  being the total and orbital angular momentum quantum numbers. The radial functions  $P_{E\kappa}(r)$  and  $Q_{E\kappa}(r)$  of Dirac spherical waves are the solutions of the coupled system of differential equations [35]

$$\frac{dP_{E\kappa}}{dr} = -\frac{\kappa}{r} P_{E\kappa}(r) + \frac{E - V + 2m_0 c^2}{c} Q_{E\kappa}(r) \quad (26)$$

and

$$\frac{dQ_{E\kappa}}{dr} = -\frac{E - V}{c} P_{E\kappa}(r) + \frac{\kappa}{r} Q_{E\kappa}(r). \quad (27)$$

The spherical waves in Equation (25) are normalized so that the large-component radial function  $P_{E\kappa}(r)$  oscillates asymptotically with unit amplitude and takes the following form

$$P_{E\kappa}(r) \sim \sin\left(kr - \ell \frac{\pi}{2} - \eta \ln 2kr + \delta_\kappa\right). \quad (28)$$

Here,  $k = \frac{p}{\hbar} = \frac{\sqrt{E(E+2m_e c^2)}}{\hbar c}$  is the relativistic wave number of the projectile and  $\eta = \frac{qe^2 m_e}{\hbar k}$  is the Sommerfeld parameter. The global phase shift  $\delta_\kappa$ , describing the large  $r$  behavior of the spherical wave solutions, is given by the following equation

$$\delta_\kappa = \Delta_\kappa + \hat{\delta}_\kappa, \quad (29)$$

with  $\Delta_\kappa$  being the Dirac-Coulomb phase shift of the potential tail and  $\hat{\delta}_\kappa$ , the complex inner phase shift caused by the complex short-range potential. Dirac-Coulomb phase shift  $\Delta_\kappa$  is given by [36]

$$\Delta_\kappa = \arg[\zeta(E + 2m_e c^2) - i(\kappa + \lambda)c\hbar k] - (\lambda - \ell - 1) \frac{\pi}{2} + \arg \Gamma(\lambda + i\eta) - S(\zeta, \kappa)\pi, \quad (30)$$

where,  $\zeta = \frac{qe^2}{\hbar c} \approx q\alpha = q/137$ ,  $\lambda = \sqrt{\kappa^2 - \zeta^2}$ , and  $S(\zeta, \kappa) = 1$  if  $\zeta < 0$  and  $\kappa < 0$ , and  $= 0$  otherwise. The phase shift  $\Delta_\kappa$  can now be used to obtain the direct and spin flip scattering amplitudes for the scattering of  $e^\pm$  from Coulomb potential  $V_{coul} = \frac{zqe^2}{r}$  as

$$f^{(C)}(\theta) = \frac{1}{2ik} \sum_{\ell=0}^{\infty} \{(\ell + 1)[\exp(2i\Delta_{-\ell-1}) - 1] + \ell[\exp(2i\Delta_\ell) - 1]\} P_\ell(\cos \theta) \tag{31}$$

and

$$g^{(C)}(\theta) = \frac{1}{2ik} \sum_{\ell=0}^{\infty} \{\exp(2i\Delta_\ell) - \exp(2i\Delta_{-\ell-1})\} P_\ell^1(\cos \theta). \tag{32}$$

To calculate the inner phase shifts  $\hat{\delta}_\kappa$ , the integration of radial equations is started at  $r = 0$  and extended outwards up to a distance  $r_m$  beyond the effective range of the interaction potential. For  $r > r_m$  the potential takes asymptotic Coulombian form and the normalized upper-component radial Dirac function can be written as

$$P_{E\kappa}(r) = \cos \hat{\delta}_\kappa f_{E\kappa}^{(u)}(r) + \sin \hat{\delta}_\kappa g_{E\kappa}^{(u)}(r). \tag{33}$$

$f_{E\kappa}^{(u)}(r)$  and  $g_{E\kappa}^{(u)}(r)$  regular and irregular Dirac–Coulomb functions, respectively. The phase shifts  $\hat{\delta}_\kappa$  can now be obtained by matching the outer analytical form to the inner numerical solution at  $r_m$ . The continuity of the radial function  $P_{E\kappa}(r)$  and its derivative is required for this boundary condition. This procedure gives

$$\exp(2i\hat{\delta}_\kappa) = \frac{D_{out}[f_{E\kappa}^{(u)}(r_m) + i g_{E\kappa}^{(u)}(r_m)] - [(f_{E\kappa}^{(u)})'(r_m) + i (g_{E\kappa}^{(u)})'(r_m)]}{[(f_{E\kappa}^{(u)})'(r_m) - i (g_{E\kappa}^{(u)})'(r_m)] - D_{out}[f_{E\kappa}^{(u)}(r_m) - i g_{E\kappa}^{(u)}(r_m)]}, \tag{34}$$

where the primes indicate the derivatives with respect to  $r$  and  $D_{out}$ , the logarithmic derivative of the outgoing numerical radial function at the matching point. The complex form of the phase shift  $\hat{\delta}_\kappa$  is due to the complex short-range potential  $V_{sr}(r)$  in Equation (3). The scattering amplitudes  $f^{sr}(\theta)$  and  $g^{sr}(\theta)$ , for the short-range potential, are given as

$$f^{sr}(\theta) = \frac{1}{2ik} \sum_{\ell=0}^{\infty} \{(\ell + 1) \exp(2i\Delta_{-\ell-1}) [\exp(2i\hat{\delta}_{-\ell-1}) - 1] + \ell \exp(2i\Delta_\ell) [\exp(2i\hat{\delta}_\ell) - 1]\} P_\ell(\cos \theta) \tag{35}$$

and

$$g^{sr}(\theta) = \frac{1}{2ik} \sum_{l=0}^{\infty} \{\exp(2i\Delta_l) [\exp(2i\hat{\delta}_l) - 1] - \exp(2i\Delta_{-l-1}) [\exp(2i\hat{\delta}_{-l-1}) - 1]\} P_l^1(\cos \theta). \tag{36}$$

Here,  $P_l(\cos \theta)$  and  $P_l^1(\cos \theta)$  are, respectively, the Legendre polynomials and associated Legendre functions.  $\theta$  is the scattering angle.

For the scattering of electrons and positrons from neutral atoms, Equation (29) reduces as  $\delta_\kappa = \hat{\delta}_\kappa$ . Therefore, the direct and spin flip scattering amplitudes can be written as

$$f(\theta) = f^{at}(\theta) = \frac{1}{2ik} \sum_{l=0}^{\infty} [l + 1] \{\exp(2i\delta_{\kappa=-l-1}) - 1\} + l \{\exp(2i\delta_{\kappa=l}) - 1\} P_l(\cos \theta) \tag{37}$$

and

$$g(\theta) = g^{at}(\theta) = \frac{1}{2ik} \sum_{l=1}^{\infty} [\exp(2i\delta_{\kappa=l}) - \exp(2i\delta_{\kappa=-l-1})] \times P_l^1(\cos \theta). \tag{38}$$

In the present MCP approach, to describe  $e^\pm$ -ion scattering, the scattering amplitudes,  $f(\theta)$  and  $g(\theta)$ , are employed as

$$f(\theta) = f^{sr}(\theta) + f^C(\theta), \quad g(\theta) = g^{sr}(\theta) + g^C(\theta). \tag{39}$$



### 2.3. Scattering Cross Sections

Once the phase shifts and the scattering amplitudes are determined, the elastic DCS per unit solid angle for unpolarized  $e^\pm$  are obtained by the following equation

$$\frac{d\sigma}{d\Omega} = |f(\theta)|^2 + |g(\theta)|^2. \tag{40}$$

In case of bare nucleus, the contributions to scattering amplitudes from short-range potential become zero and, therefore, the DCS per unit solid angle for the elastic scattering of  $e^\pm$  by the bare radon is calculated using

$$\frac{d\sigma}{d\Omega} = |f^C(\theta)|^2 + |g^C(\theta)|^2. \tag{41}$$

The initially unpolarized  $e^\pm$  beam becomes polarized after being scattered in the direction  $\theta$ . The degree of this spin polarization is given by Sherman function [37]

$$S(\theta) \equiv i \frac{f(\theta)g^*(\theta) - f^*(\theta)g(\theta)}{|f(\theta)|^2 + |g(\theta)|^2}. \tag{42}$$

The integrated elastic, momentum transfer, viscosity, total and inelastic cross sections are defined by the following respective expressions

$$\sigma_{el} = \int \frac{d\sigma}{d\Omega} d\Omega = 2\pi \int_0^\pi (|f(\theta)|^2 + |g(\theta)|^2) \sin(\theta) d\theta, \tag{43}$$

$$\sigma_m = 2\pi \int_0^\pi (1 - \cos\theta) \left( \frac{d\sigma}{d\Omega} \right) \sin(\theta) d\theta, \tag{44}$$

$$\sigma_v = 3\pi \int_0^\pi [1 - (\cos\theta)^2] \left( \frac{d\sigma}{d\Omega} \right) \sin(\theta) d\theta, \tag{45}$$

$$\sigma_{tot} = \frac{4\pi}{k} \text{Im}f(0) \tag{46}$$

and

$$\sigma_{ine} = \sigma_{tot} - \sigma_{el} \tag{47}$$

Here,  $\text{Im}f(0)$  denotes the imaginary part of the direct scattering amplitude in the forward direction at  $\theta = 0$ .

The Coulomb glory effect is estimated by scaling DCS in Equation (40) as [38]

$$\frac{d\tilde{\sigma}}{d\Omega} = \left( \frac{4E}{q} \right)^2 \frac{d\sigma}{d\Omega} \tag{48}$$

The scaled Rutherford differential cross section (SRCS), independent of energy and ionic charge, is given as

$$\frac{d\tilde{\sigma}^c}{d\Omega} = \frac{1}{\sin^4 \theta/2}. \tag{49}$$

The value of SRCS is unity at  $180^\circ$  and hence the scaled differential cross section (SDCS),  $\frac{d\tilde{\sigma}}{d\Omega}$  in Equation (48) represents the ratio of  $e^-$ -ion DCS and corresponding Rutherford DCS at  $\theta = 180^\circ$ .

### 3. Numerical Analysis

In Figure 1a,b, we present  $r$ -dependence real part of the short-range potential  $V_{sr}$  as well as the Coulomb potential  $V_c$  both for electron and positron projectiles. We present separately the contribution of static potential  $V_{st}(r)$ , because it dominates the optical potential. All of these potentials are plotted as a function of distance  $r$  from the nucleus. The



Bohr radius  $a_0 = \frac{\hbar^2}{me^2} = 1$  a.u., and the location of the  $n^{\text{th}}$  electronic shell is approximated as

$$r = a_0 \frac{n^2}{Z}. \tag{50}$$

It is worth mentioning that, due to the presence of the exchange and the absorption part in optical potential, there are some dependence on the collision energy, and the potentials shown in Figure 1 are calculated for 1 keV. The nuclear radius of radon is  $\simeq 1.4 \times 10^{-4}$  a.u. At  $r < 10^{-4}$  a.u., the nuclear potential accounts for the finite nuclear size and is derived from the Fermi charge distribution. As in Figure 1a, the electronic potential coincides with the Coulomb field in the region  $r \lesssim 10^{-3}$  a.u., i.e., outside the nucleus, but well inside the K-shell. The respective potentials for positron scattering are shown in Figure 1b. Due to opposite charge of the projectile the optical potential for positron scattering has basically a sign reversal as compared to the electronic potential.

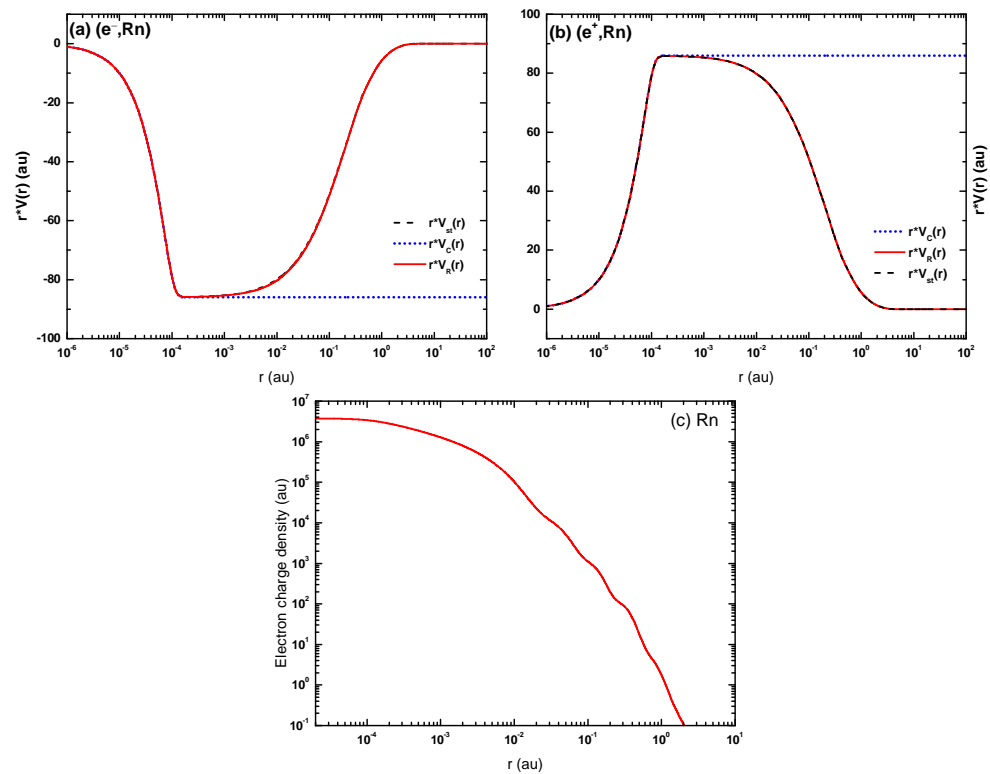


**Figure 1.** Potentials (multiplied by  $r$ ) for electrons (a) and positrons (b) as a function of distance  $r$  from the nucleus. Shown are the real part  $V_R$  (—, red) and its static part  $V_{st}$  (---, black) of the short range OPM potential. The Coulomb field  $V_C = -Z/r$  is also included (⋯⋯⋯, blue). In (c) shown is the  $r$  dependence of electron charge density.

Figure 1c displays the  $r$ -dependence of electronic number density  $\rho_e$  for the radon atom. This figure demonstrates clearly the electronic shell structure as well as the positions of hump appearing in the density distribution. From Equation (50), one gets  $r \approx 0.016, 0.065, 0.147$  and  $2.344$  a.u., respectively, for the K-, L-, M- and N-shells, which agree nicely with the humps in the corresponding density. Two more humps are present in  $\rho_e$ , the positions of which are, however, underpredicted by the above formula since there are only 18 and 8 electrons in the O and P-shells, respectively.

Figure 2 demonstrates the sensitivity of different constituents of the real part of  $V_{sr}$  used in the present study to predict DCS and  $S(\theta)$  both for electrons and positrons scattering from  $^{222}\text{Rn}$  atoms. For a sample case the energy dependence of the DCS and of the  $S(\theta)$  are given at the scattering angle  $\theta = 90^\circ$ , proceeding from  $V_{st}$  to  $V_{opt}$  by successively including  $V_{ex}$ ,  $V_{cp}$  and  $W_{abs}$ . It is evident from this figure that the static potential  $V_{st}$  is the dominant

contributor to both DCS and  $S(\theta)$  over the entire energy range. The remaining components (i.e., the exchange  $V_{ex}$ , the polarization  $V_{cp}$  and the absorption  $W_{abs}$ ) have very small contribution except at lower energies. For electron impact scattering, in Figure 2a,b, the inclusion of the  $V_{ex}$  leads to a considerable modification of the structures both in DCS and  $S(\theta)$ . Furthermore, this influence of  $V_{ex}$  remains important up to 100 eV for the DCS and 50 eV for the  $S(\theta)$ . Due to the absence of  $V_{ex}$ , the DCS and  $S(\theta)$  for positron scattering, in Figure 2c,d, show monotonous behavior. This behavior indicates that the atomic electrons just screen the nuclear field in the case of positron impact, while they act as individual scattering centers for electron scattering.

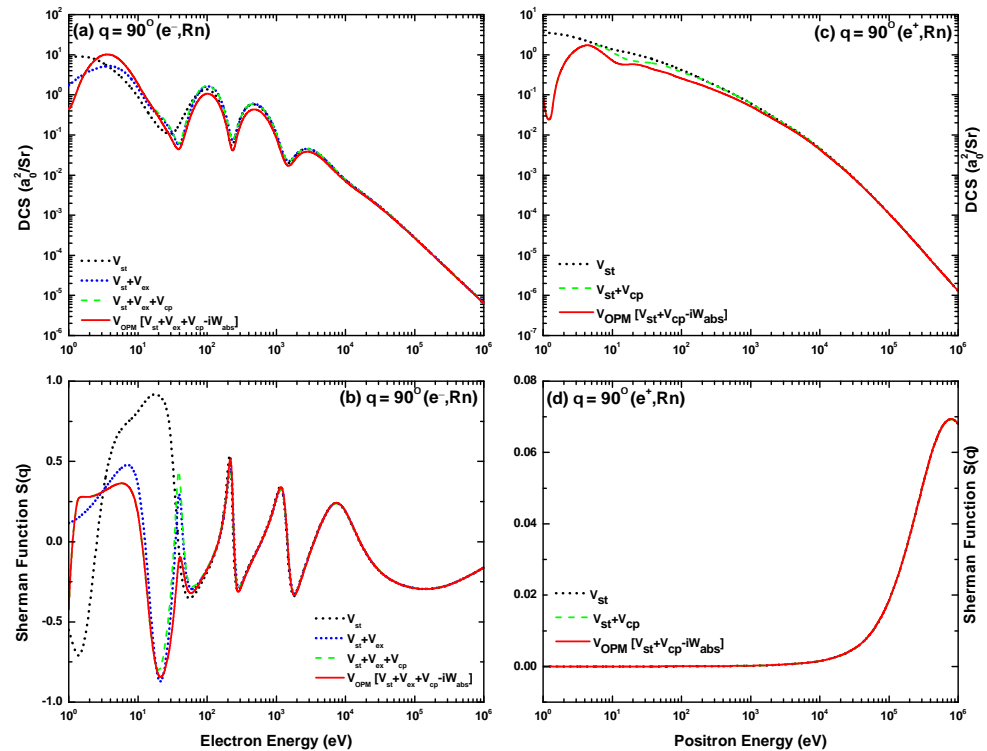


**Figure 2.** Energy dependence of (a,c) the DCS and (b,d) the Sherman function  $S(\theta)$  for electron (a,b) and positron (c,d) impact on  $^{222}\text{Rn}$  at a scattering angle of  $90^\circ$ . Shown are the results ( $\cdots$ , black) from  $V_{st}$ ; ( $\cdots$ , blue) from  $V_{st} + V_{ex}$ ; ( $---$ , green) from  $V_R = V_{st} + V_{ex} + V_{cp}$  and  $V_R = V_{st} + V_{cp}$ , respectively, for electron and positron projectiles; and ( $---$ , red) from  $V_{opt} = V_{st} + V_{ex} + V_{cp} - iW_{abs}$  for electron scattering and  $V_{opt} = V_{st} + V_{cp} - iW_{abs}$  for positron scattering, respectively.

The polarization potential  $V_{cp}$  contributes significantly only at energies below 10 eV and its contribution decreases rapidly at higher energies. At this lower energies, the  $V_{cp}$  counteracts  $V_{ex}$  by reducing the excursions in the DCS and in  $S$ . However, for positron scattering, the  $V_{cp}$  induces some minor modulations into the monotonous DCS and  $S(\theta)$  at  $E_i = 10\text{--}100$  eV. The absorption potential  $W_{abs}$  diminishes the contribution of  $V_{st}$  starting from the ionization threshold ( $\sim 10$  eV) and continues up to 5 keV for the DCS, but up to 100 eV for the  $S(\theta)$ . It is worth mentioning that the magnitudes of both the DCS and  $S(\theta)$  are several fold lower for positron projectile signifying that the positron scattering is rather weaker as compared to its electron counterpart.

In Figure 3, we present DCS and Sherman function for 50–5000 eV electrons impact on  $^{222}\text{Rn}$  to demonstrate the effect of different contributions to the  $V_{st}$ . One can notice, from Figure 3a at 50 eV, a significant difference between the DCS results from  $V_{st}$  and  $V_{opt}$ , particularly in the forward hemisphere. This is due to the greater influence of the other potential constituents on the cross section at lower energies than so at higher energies. The absorption potential remains important at energies up to about 500 eV, decreasing the DCS

by up to a factor of 2. Even at 5 keV, its influence is still visible. Comparison is also made with the result for a pure Coulomb field  $V_C$ , for which the DCS diverges at zero angle. It is seen that the  $V_{sr}$  results gradually approach the Coulombic behavior with increasing energy. This happens due to the deeper penetration of the projectile at higher energies and thereby making the effect of the screening of the nucleus by the surrounding electrons lesser and lesser.

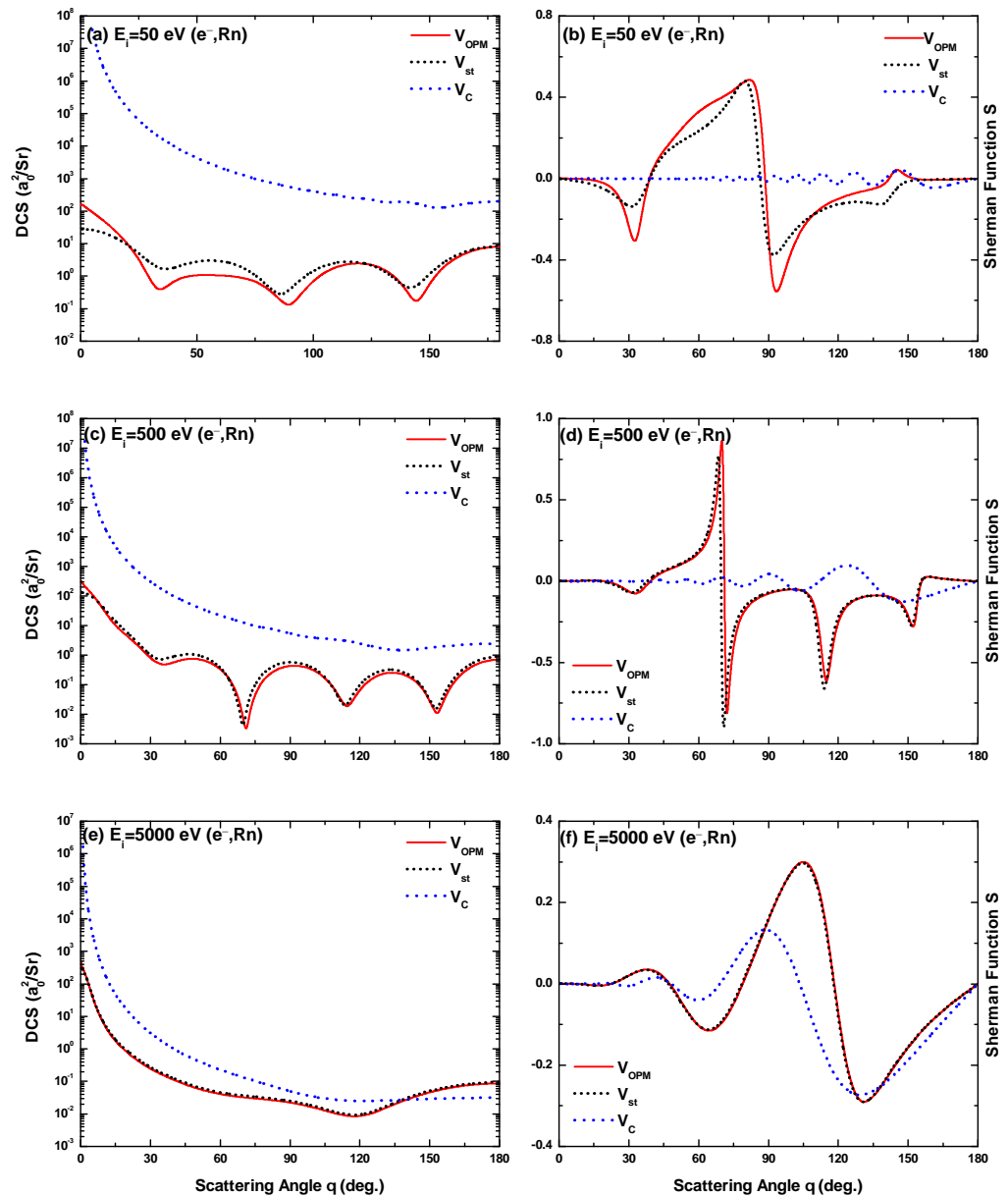


**Figure 3.** Angular dependence of (a,c,e) the DCS and (b,d,f) the Sherman function for electrons at 50 eV (a,b), 500 eV (c,d) and 5000 eV (e,f) colliding with  $^{222}\text{Rn}$ . Shown are the results from  $V_{st}$  (· · ·, black) and  $V_{opt}$  (—, red). Included also are the results for the Coulomb field  $V_C$  (· · ·, blue).

As concerns the Sherman function with its three resonance structures at the DCS minima, the sign of the excursion is conserved at the first two structures, but reversed at the third one when other contributions are added to  $V_{st}$ . With increasing energy, oscillatory behavior of the Sherman function from the Coulomb field gradually matches the respective behavior induced by the full  $V_{sr}$  potential. Figure 4 displays the respective results for positron impact. The correlation-polarization potential induces oscillations both in the DCS and in  $S(\theta)$  at small energies. The influence of the absorption potential is even stronger than

for electrons, particularly for the spin asymmetry. Furthermore, the Coulombic behavior is not yet approached at 5 keV.

Figure 5 displays energy dependence of the DCS and the Sherman function for  $e^{\pm} \text{ } ^{222}\text{Rn}$  scattering comparing the predictions of the  $V_{st}$  and  $V_{sr}$  with those of the Coulomb field  $V_C$ . For electron impact scattering, as seen in Figure 5a, the differences between the DCS results predicted by  $V_{sr}$  and those by  $V_C$  gradually decrease with increasing energy, and almost vanish at energies beyond 10 keV. In the case of  $S(\theta)$ , in Figure 5b, the oscillatory behavior induced by these two potentials gradually matches with increasing incident energies. Same features are observed for the positron impact scattering as evident in Figure 5c,d. However, the differences between the DCS results predicted by these two potentials persist in more higher energies (50 keV) indicating that the influence of the absorption potential is even stronger than for electrons.

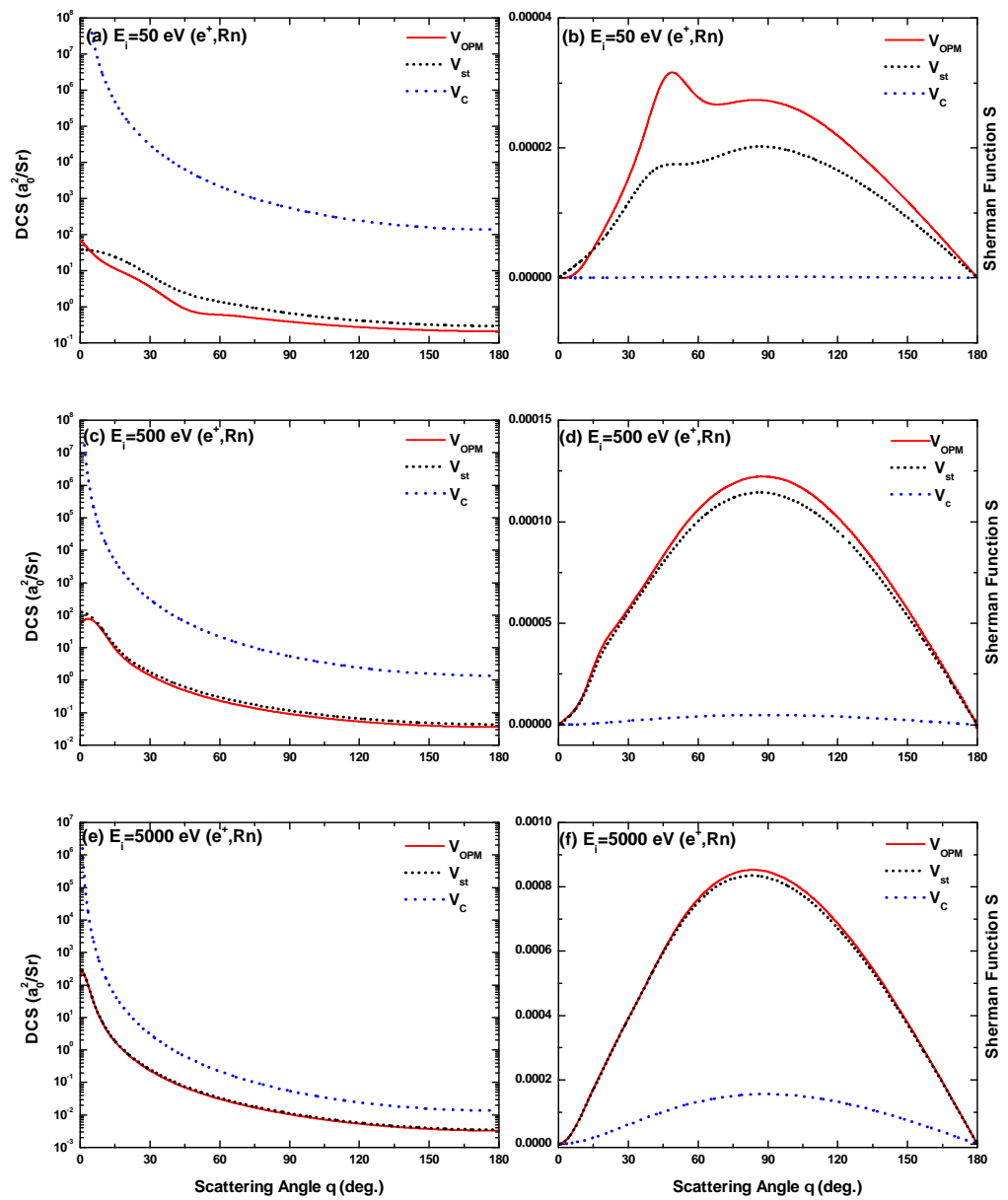
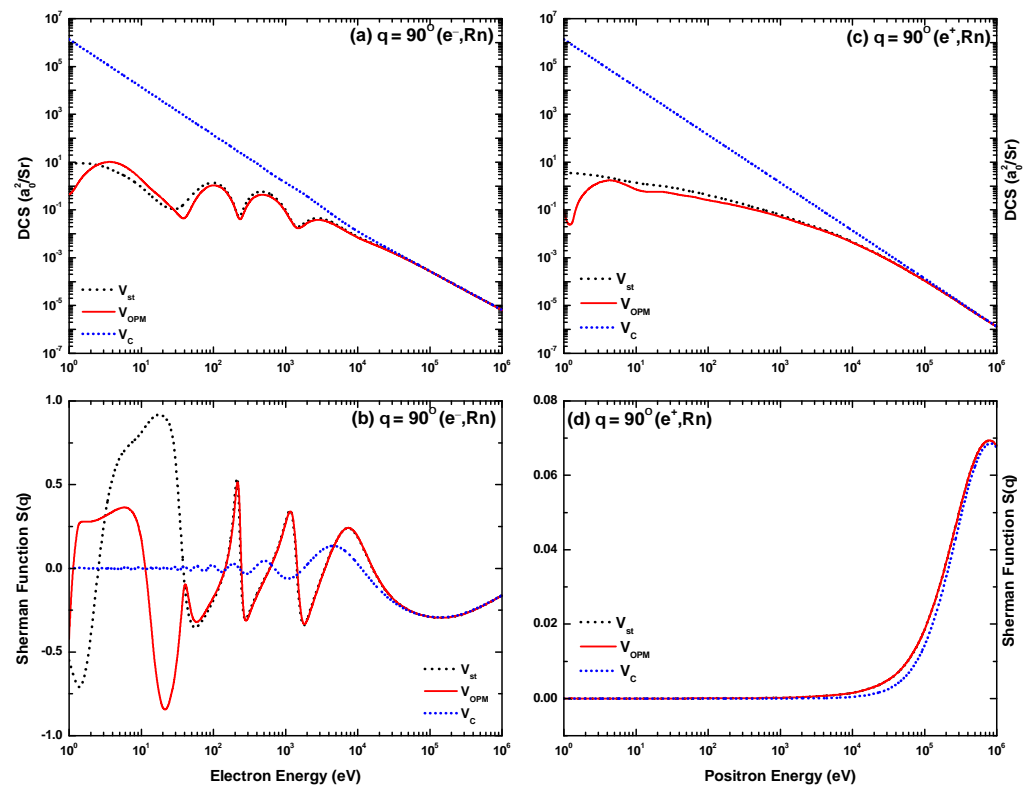


Figure 4. Same as Figure 3, but for the positron impact scattering.



**Figure 5.** Energy dependence of (a,c) the DCS and (b,d) the Sherman function  $S(\theta)$  for electron (a,b) and positron (c,d) impact scattering from  $^{222}\text{Rn}$  at a scattering angle of  $90^\circ$ . Shown are the results from  $V_{\text{st}}$  (·····, black),  $V_{\text{opt}}$  (—, red) and  $V_{\text{C}}$  (·····, blue).

## 4. Results and Discussion

### 4.1. Electron Scattering from Neutral Radon

The DCS for electrons elastically scattered from neutral radon calculated using our modified Coulomb potential over a wide range of energies  $10 \text{ eV} \leq E_i \leq 10 \text{ keV}$  are presented in Figures 6–9. As seen in these figures, the number of minima in the present DCS distributions varies with energy from 1 at  $E_i = 10 \text{ eV}$  to 3 at  $20 \leq E_i \leq 200 \text{ eV}$  and to 4 at  $300 \leq E_i \leq 700 \text{ eV}$ . The DCS again reveals 3 minima at  $900 \leq E_i \leq 1000 \text{ eV}$  and 2 at  $1500 \leq E_i \leq 5000 \text{ eV}$ . With a further increase in the collision energy to  $E_i \geq 6000 \text{ eV}$ , the number of minima reduces to 1. These minima in the cross sections, the so-called Ramsauer–Townsend (R-T) structures [39], are due to diffraction effects arising from the quantum-mechanical nature of matter. The R-T structures disappear when the collision becomes so energetic that the lepton-atom interactions occur inside the K-shell. These structures are, therefore, of great interest to study collision dynamics.

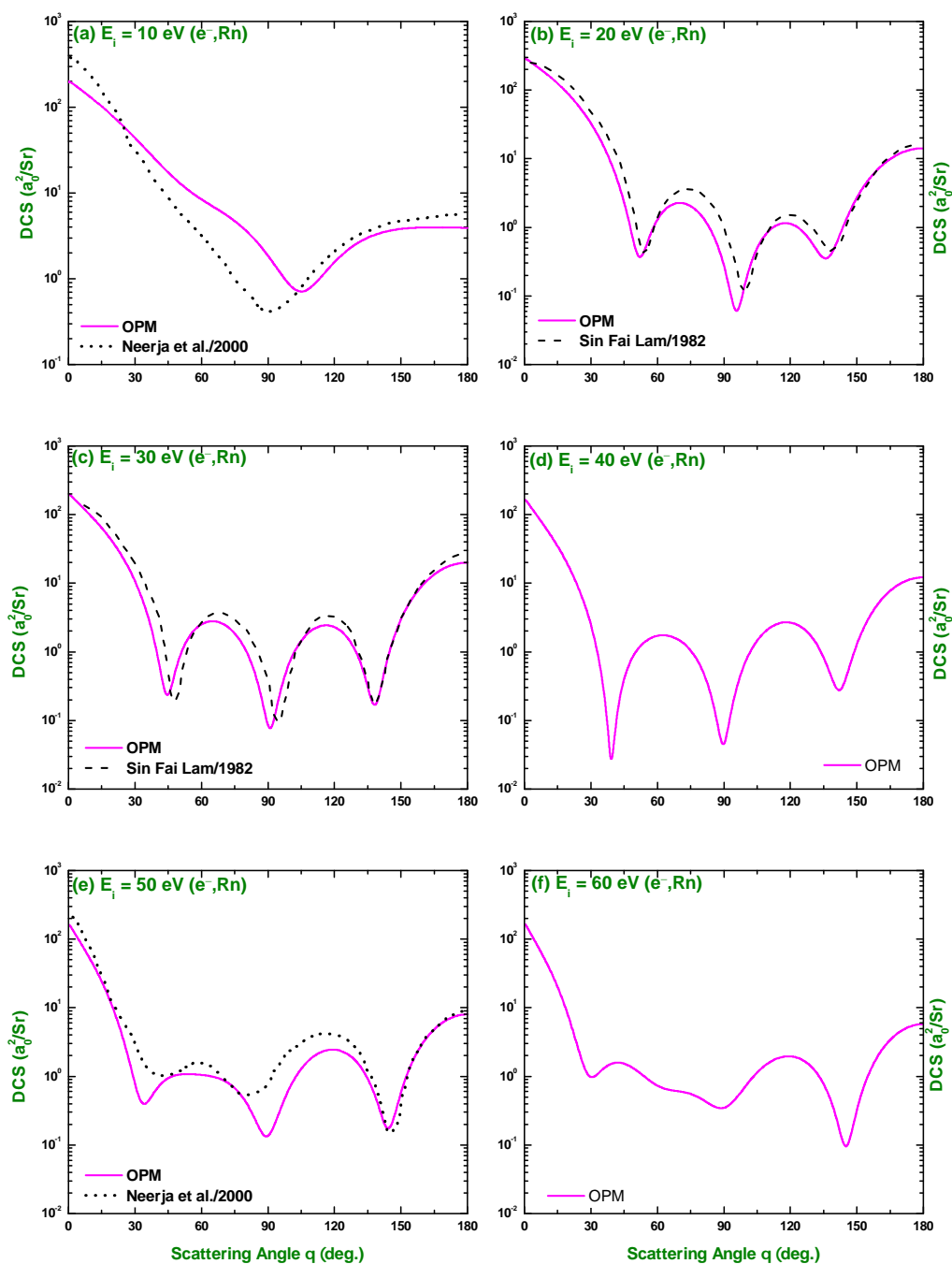


**Figure 6.** Angular dependence of the differential cross section of electrons scattering from  $^{222}\text{Rn}$  at impact energies  $E_i = 10, 20, 30, 40, 50$  and  $60$  eV. Shown are the results from our MCP (—), Neerja et al. [19] (⋯⋯⋯) and Sin Fai Lam [13] (---).

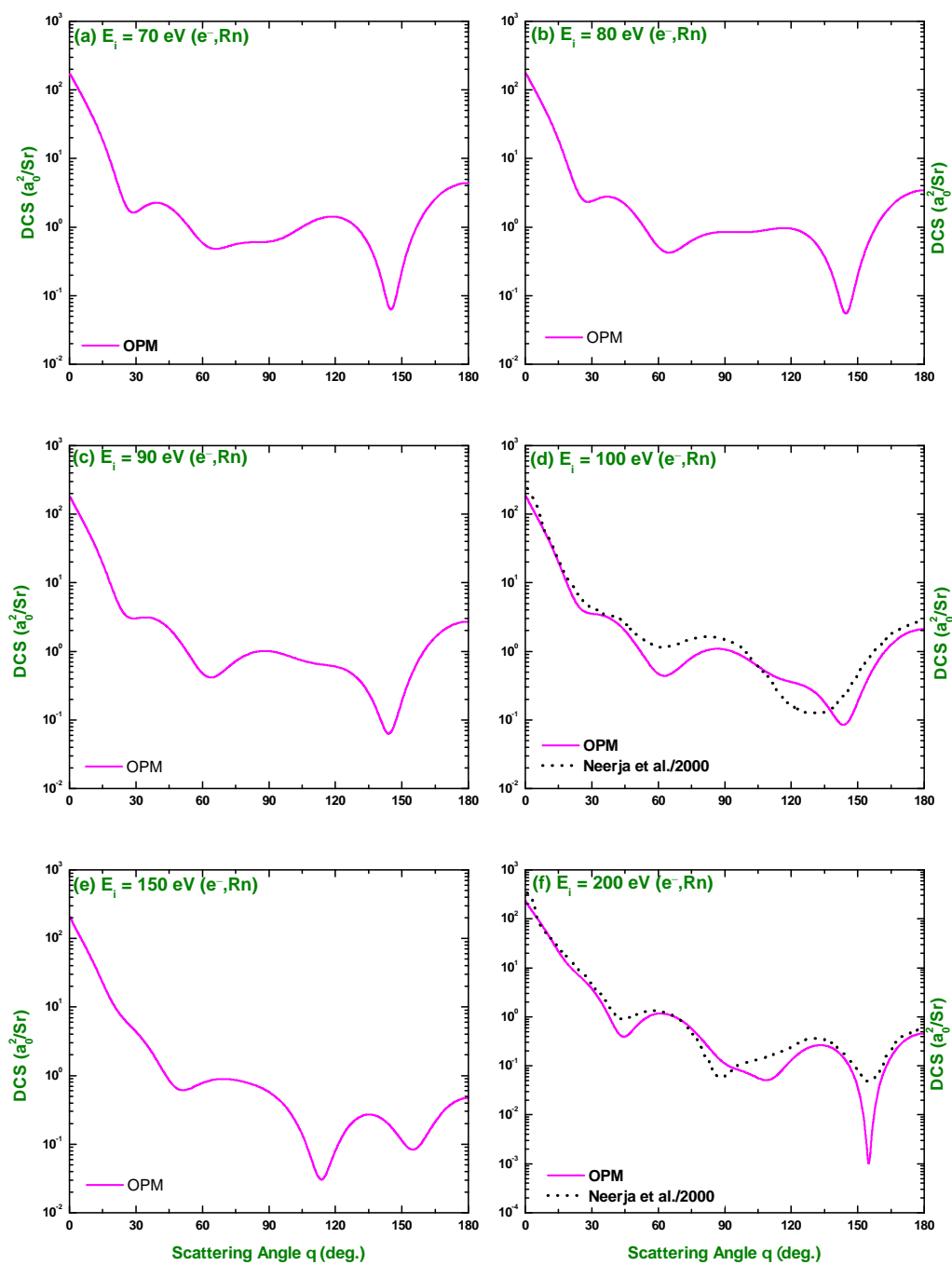


**Figure 7.** Angular dependence of the differential cross section of electrons scattering from  $^{222}\text{Rn}$  at  $E_i = 70, 80, 90, 100, 150$  and  $200$  eV. Included are the results from Neerja et al. [19] ( $\cdots$ ) at  $100$  and  $200$  eV.



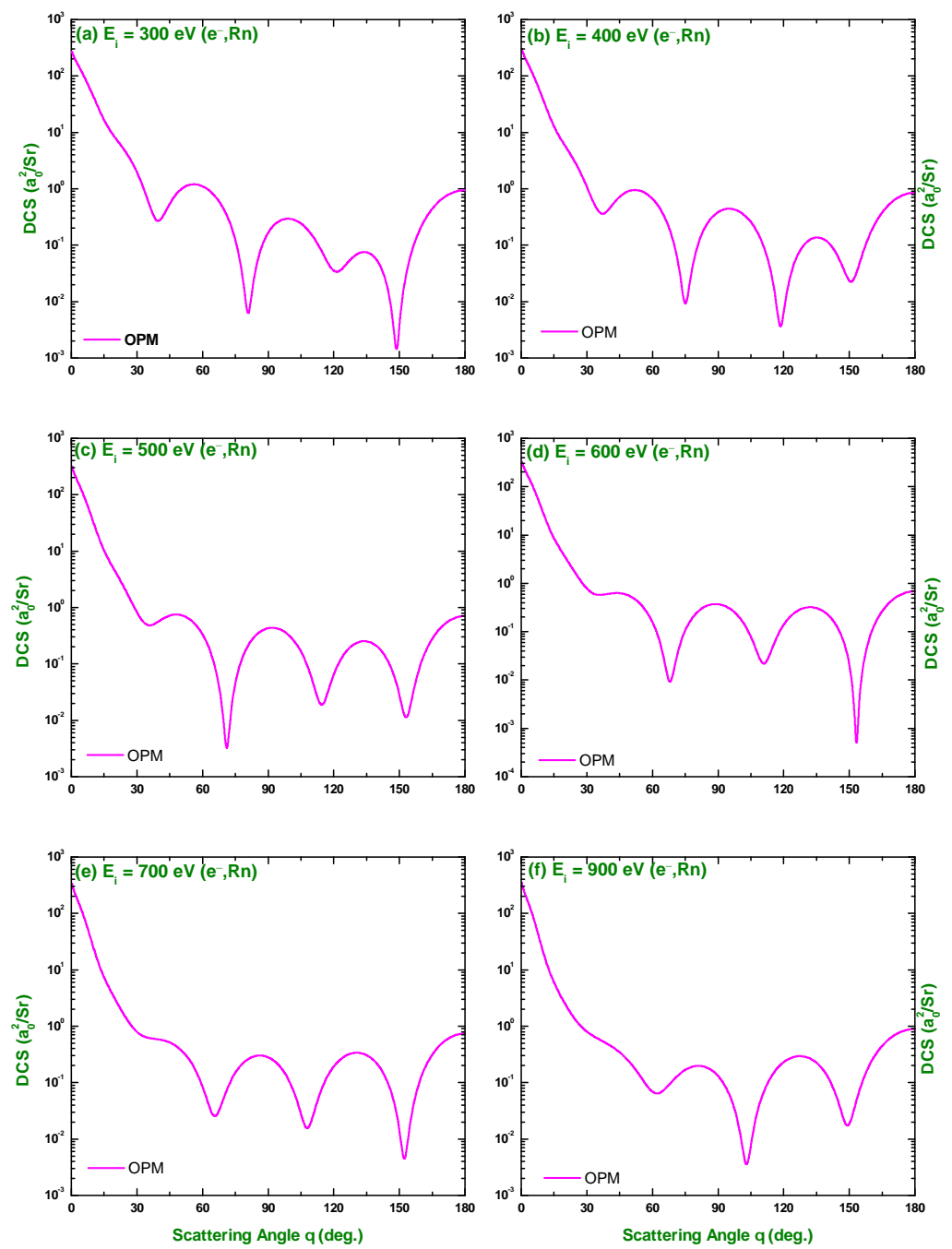


**Figure 8.** Angular dependence of the differential cross section of electrons scattering from  $^{222}\text{Rn}$  at  $E_i = 300, 400, 500, 600, 700$  and  $900 \text{ eV}$ .

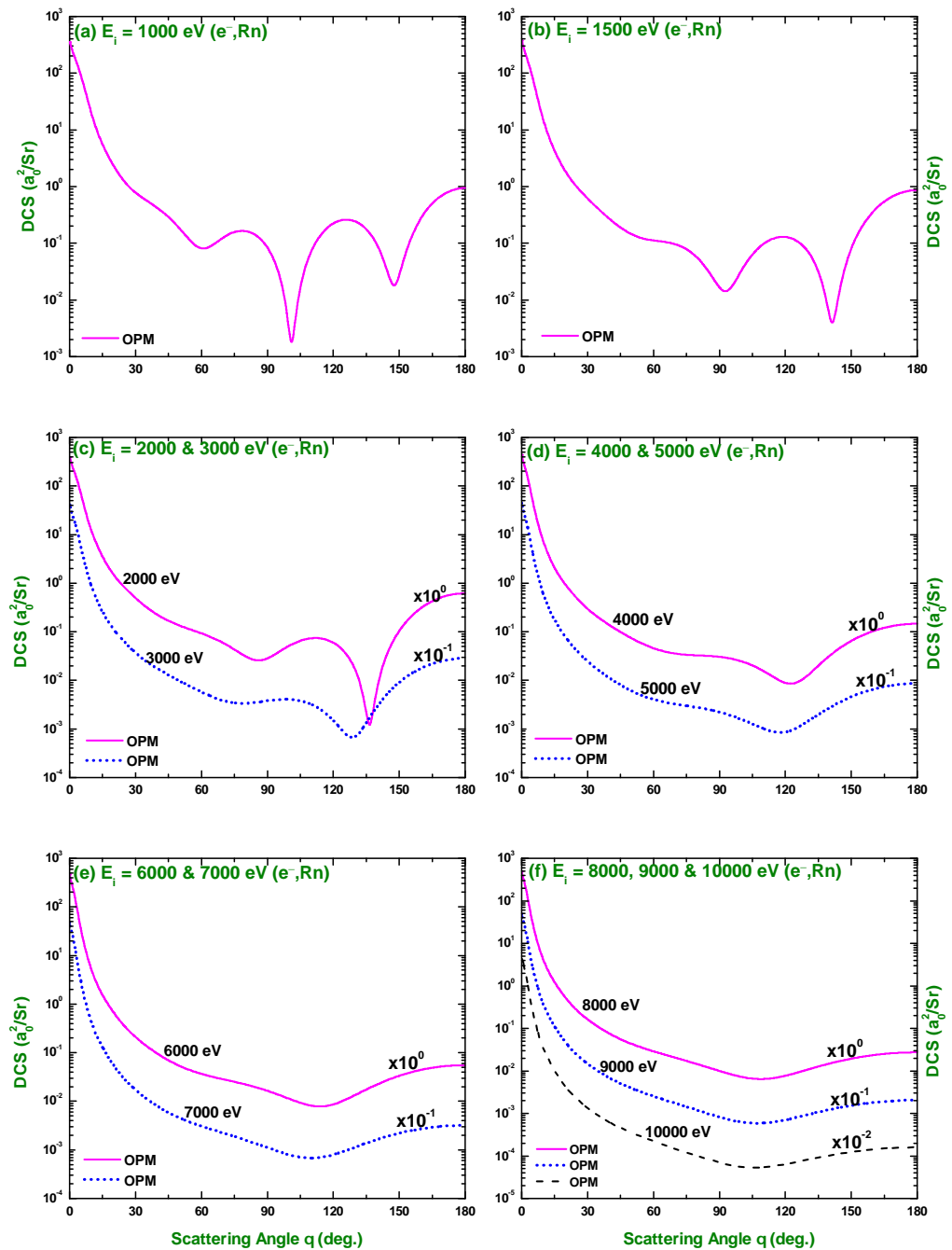


**Figure 9.** Angular dependence of the differential cross section of electrons scattering from  $^{222}\text{Rn}$  at  $1 \leq E_i \leq 10$  keV.

As there is no experimental data for this scattering system, we compare our DCS results with the optical model calculations of Neerja et al. [19] available at 10–200 eV and semi-relativistic calculations of Sin Fai Lam [13] at 20–30 eV. For  $E_i \geq 300$  eV, we have found neither any experimental nor other theoretical results to compare with. We anticipate that the present results might be useful for applications and comparisons for future experimental as well as theoretical studies. The comparison, where possible, revealed that the three methods exhibit oscillations at about the same scattering angles but with little differences in the magnitude. These differences signify the sensitivity of the theoretical models involving different interaction potentials. It is worth mentioning that Neerja et al. [19] used optical potential but without the long-range Coulomb potential. The poor agreement of our results with those of [19], at 10 eV in Figure 6a, may be due to the onset of the inelastic threshold

that interplay between the real and imaginary components of the optical potential due to dispersion.

In Figures 10–12, we present our MCP results of the Sherman function  $S$  for  $e^-$ - $^{222}\text{Rn}$  scattering at incident energies  $10 \leq E_i \leq 1000$  eV. One can see in these figures that the minima in  $S(\theta)$  are strongly related to the minima in the DCS distributions. However, the structures in  $S(\theta)$  are much more pronounced than those in the DCS. This is expected because the spin asymmetry is more sensitive to the choice of potentials and methods of calculations. It is also evident that, at low energies ( $E_i \leq 100$  eV), the magnitudes of  $|S|$  are higher at forward scattering angles than at backward angles. This is due to the effect of the exchange potential that deepens the minima, but is less important at backward angles. In contrast, at higher energies ( $\geq 150$  eV), the magnitude of  $|S|$  gets larger with increasing scattering angle. This is the effect of the stronger nuclear field on the spin polarization at the smaller projectile-nucleus distance.

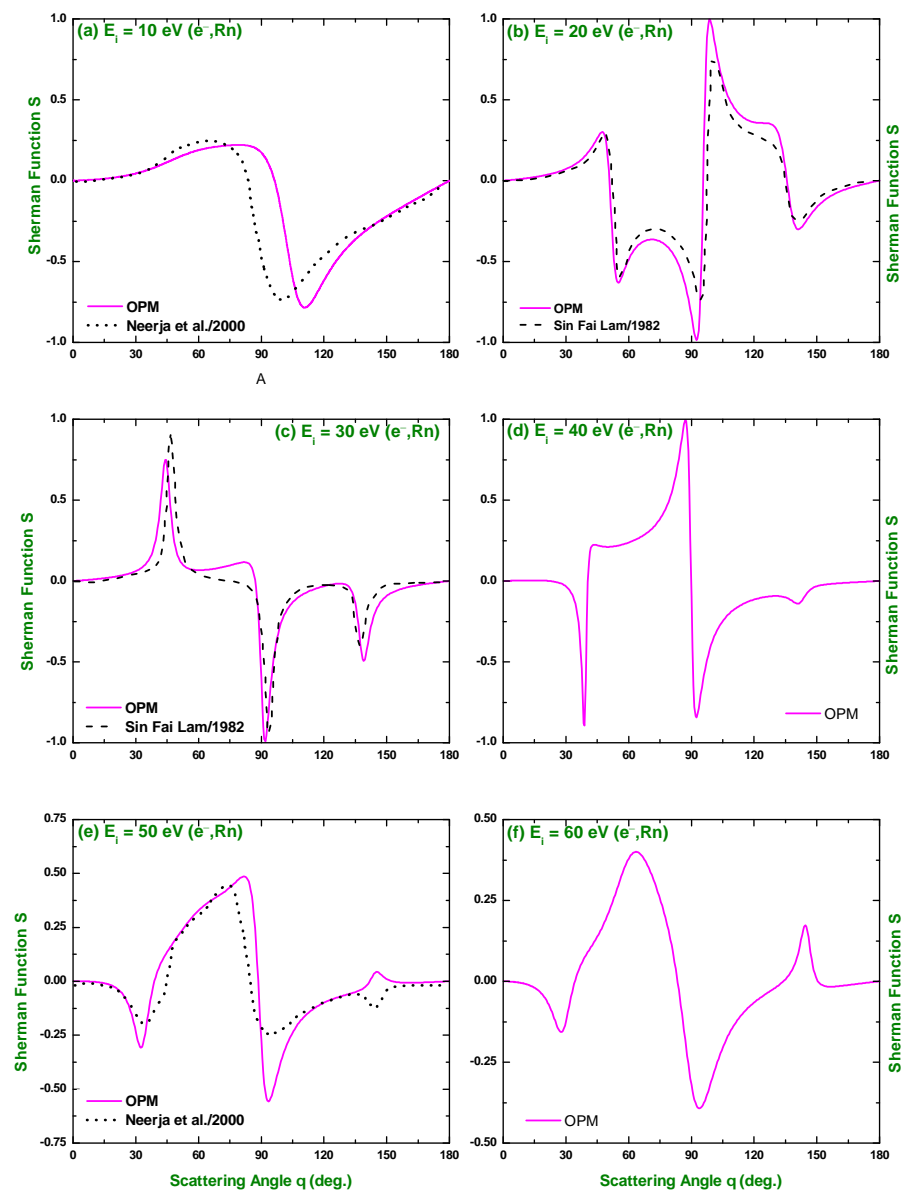


**Figure 10.** Angle dependent Sherman function  $S$  for elastic scattering of 10, 20, 30, 40, 50 and 60 eV electrons from neutral radon atoms: — curves, present calculations (MCP); ····· curves, ref. [19] and - - - curves, Ref. [13].

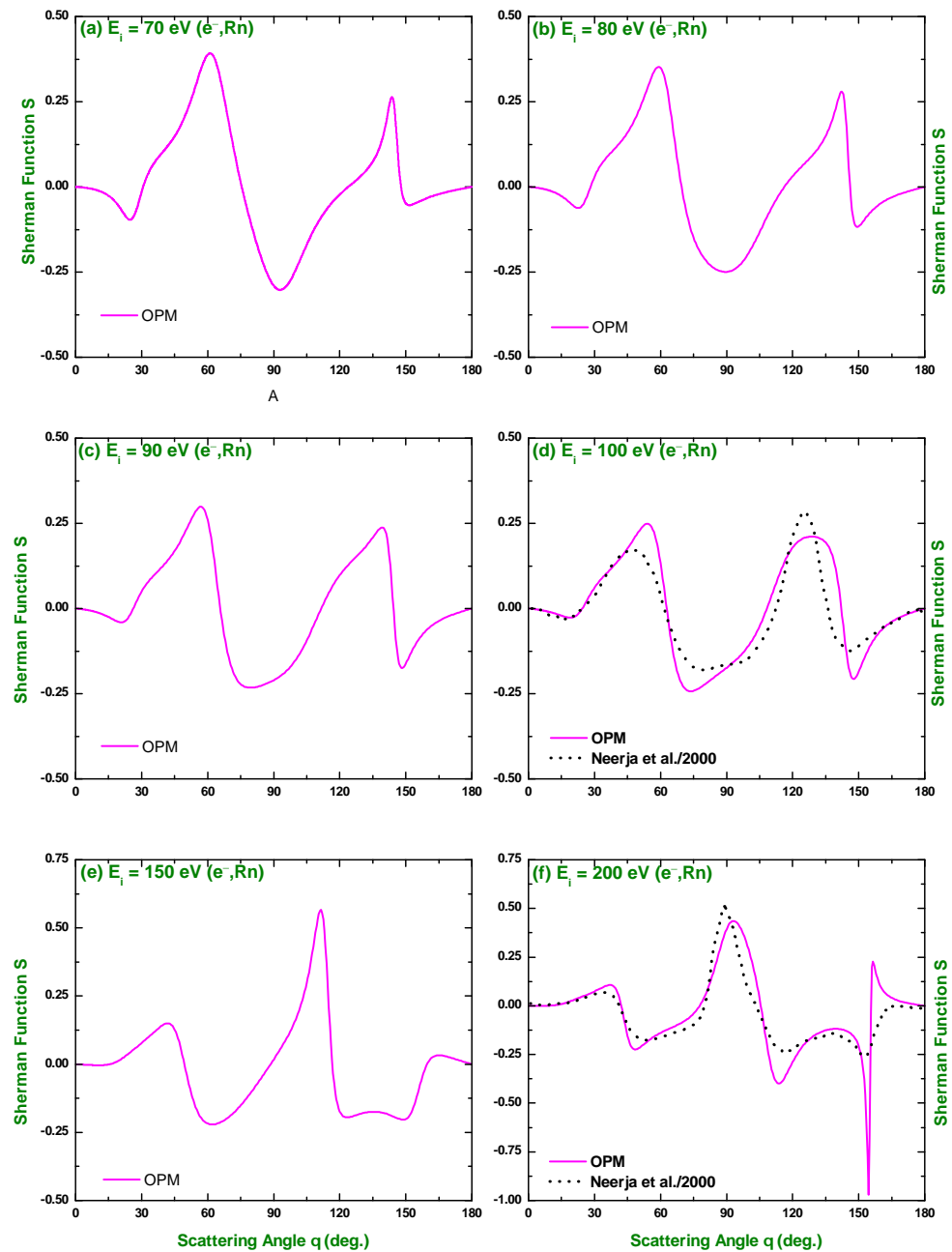


Figure 11. Same as Figure 10, but at impact energies of 70, 80, 90, 100, 150 and 200 eV.

Because of the absence of any experimental data we compare our  $S$  results again with the calculations of Neerja et al. [19], available at 10, 50, 100 and 200 eV, and of Sin Fai Lam [13], available at 20 and 30 eV. Similar to the DCS comparison, one can observe that these three calculations of Sherman function agree closely with one another with the deviations as follows: (i) a tiny differences in magnitude of  $|S|$  at the minima or maxima positions, (ii) at 10 eV, present method predicts a minimum at  $110^\circ$ , while that from [19] is observed at  $100^\circ$ , (iii) at 50 eV, the third extremum predicted by the present method and that of Neerja et al. [19] are opposite in sign. All of these differences might be attributed due to the different components of optical potentials used in these two methods as already mentioned earlier. More data and calculations might be helpful to shed light on the presence of these discrepancies.

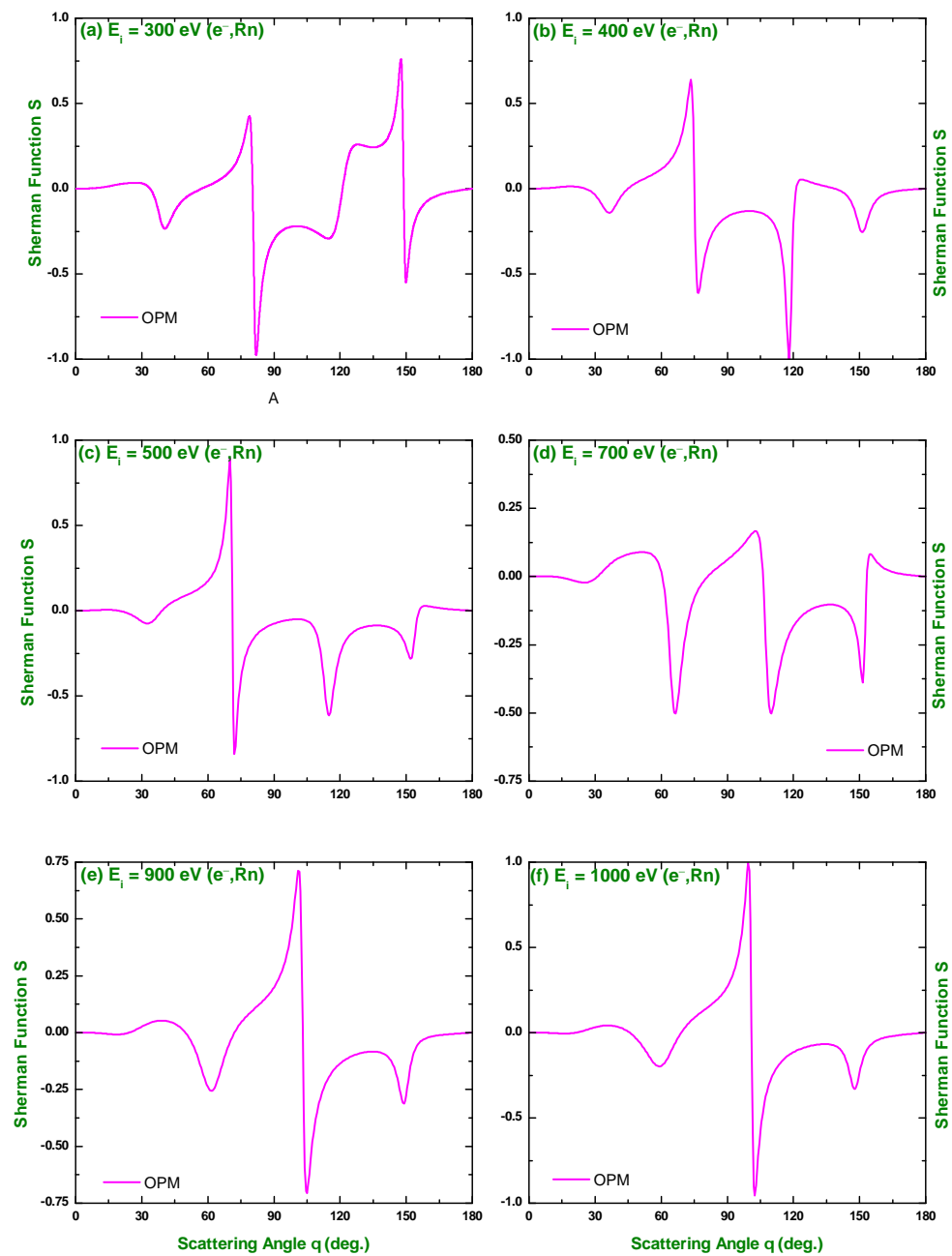
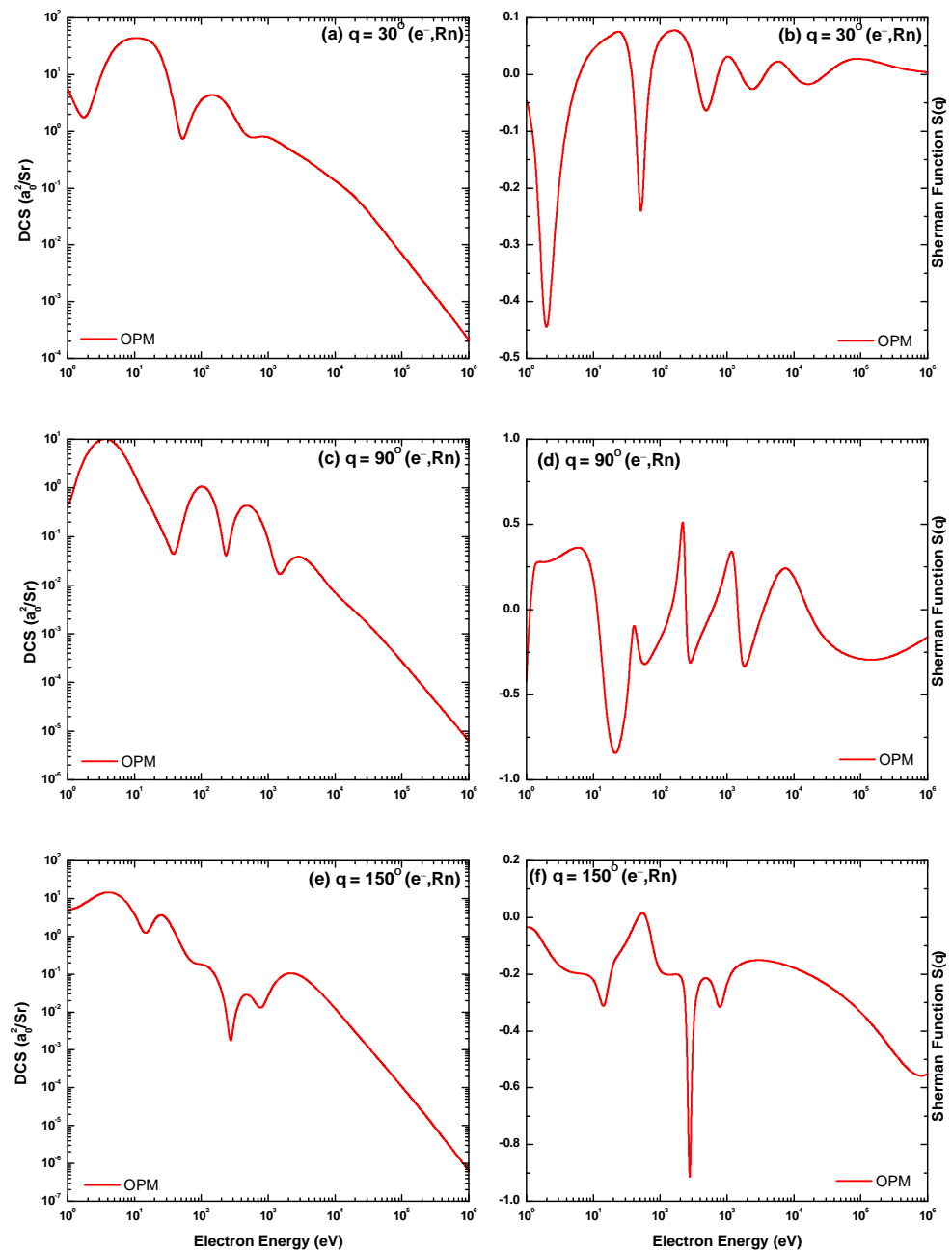


Figure 12. Same as Figure 10, but at impact energies of 300, 400, 500, 700, 900 and 1000 eV.

Figure 13 displays the energy dependence of the DCS and Sherman function of the elastic  $e^{-222}\text{Rn}$  scattering over the energy range  $1 \text{ eV} \leq E_i \leq 1 \text{ MeV}$  at two forward scattering angles ( $\theta = 30^\circ$  and  $90^\circ$ ) and one backward angle ( $\theta = 150^\circ$ ). This figure (panels a, c and e) clearly demonstrates that strong R-T structures are present in the DCSs at all scattering angles for kinetic energies  $E_i < 3 \text{ keV}$ . It is also revealed that the R-T structures gradually fade out as  $E_i$  approaches towards the M-subshells binding energies (3–4.6 keV [40]). Beyond 3 keV, the DCS declines monotonously with  $E_i$ . This is expected because the pure Coulomb field of the nucleus dominates in this energy regime.



**Figure 13.** Energy dependence of the DCS and the Sherman function for elastic scattering of electrons from neutral radon atoms at scattering angles (a,b): 30°, (c,d): 90° and (e,f): 150°.

The energy variation of the corresponding Sherman function (panels b, d and f in Figure 13) shows that the magnitude of  $|S|$  increases with the increase of scattering angles  $\theta$ . The appearance of the structure continues up to more energies at lower scattering angles than at higher one. However, the position of the highest extremum is shifted to higher energies with increasing the scattering angles. All of these features might be explained as the fact that the exchange potential, which significantly affects the minima, has less influence in the backward direction. For high energies, on the other hand, due to the smaller projectile-nucleus distance, the stronger nuclear field has a significant effect on the spin polarization implying that the magnitude of  $|S|$  increases with increasing scattering angle.

Figure 14 depicts the energy variation of additional polarization parameters  $U(\theta)$  and  $T(\theta)$  at few selected angles ( $\theta = 30^\circ, 90^\circ$  and  $150^\circ$ ). The complete dependence of the scattering process on the spin variables can be obtained from these parameters, where

$$U = \frac{2\text{Im}f(\theta)g^*(\theta)}{|f(\theta)|^2 + |g(\theta)|^2} \quad (51)$$

and

$$T = \frac{|f(\theta)|^2 - |g(\theta)|^2}{|f(\theta)|^2 + |g(\theta)|^2} \quad (52)$$

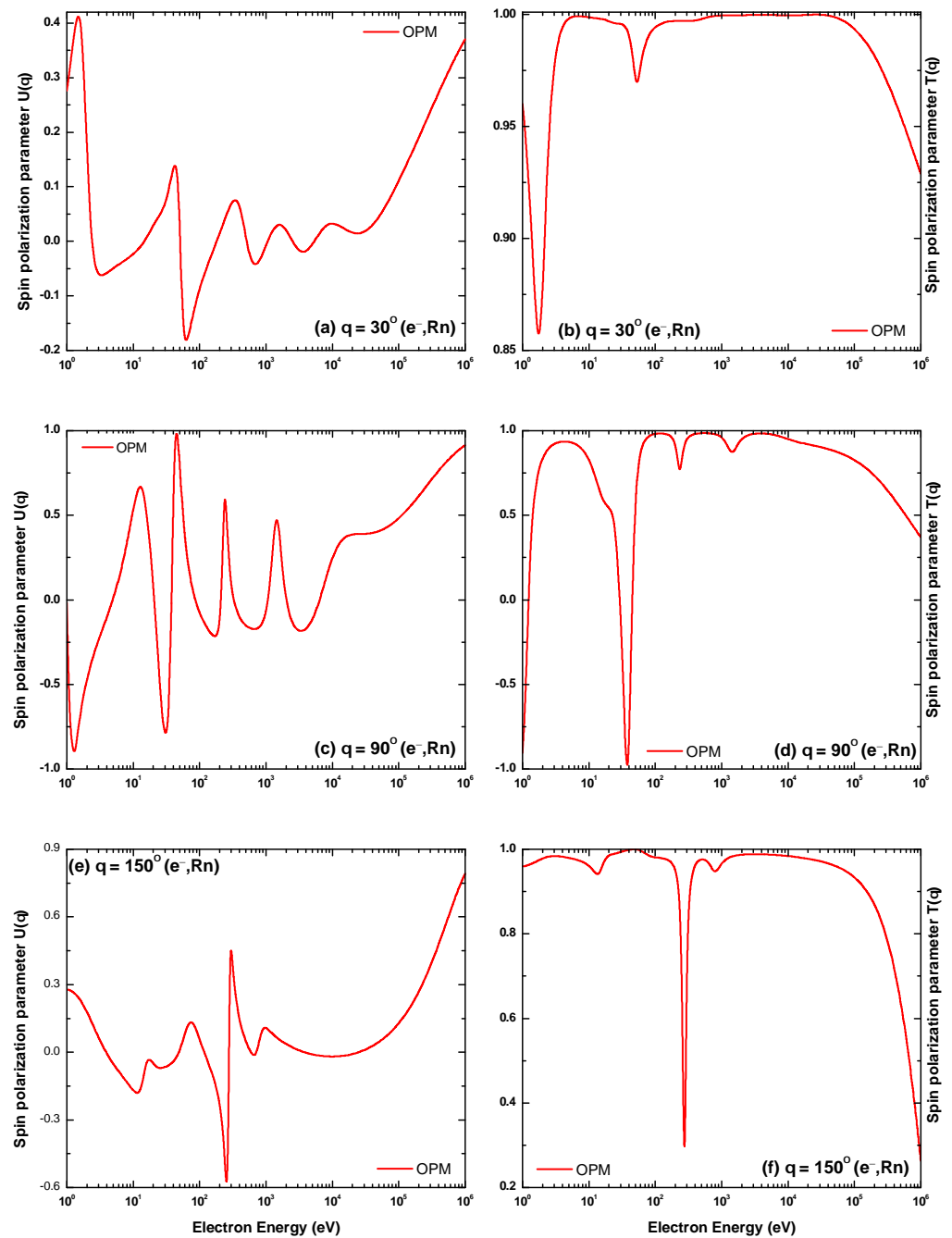
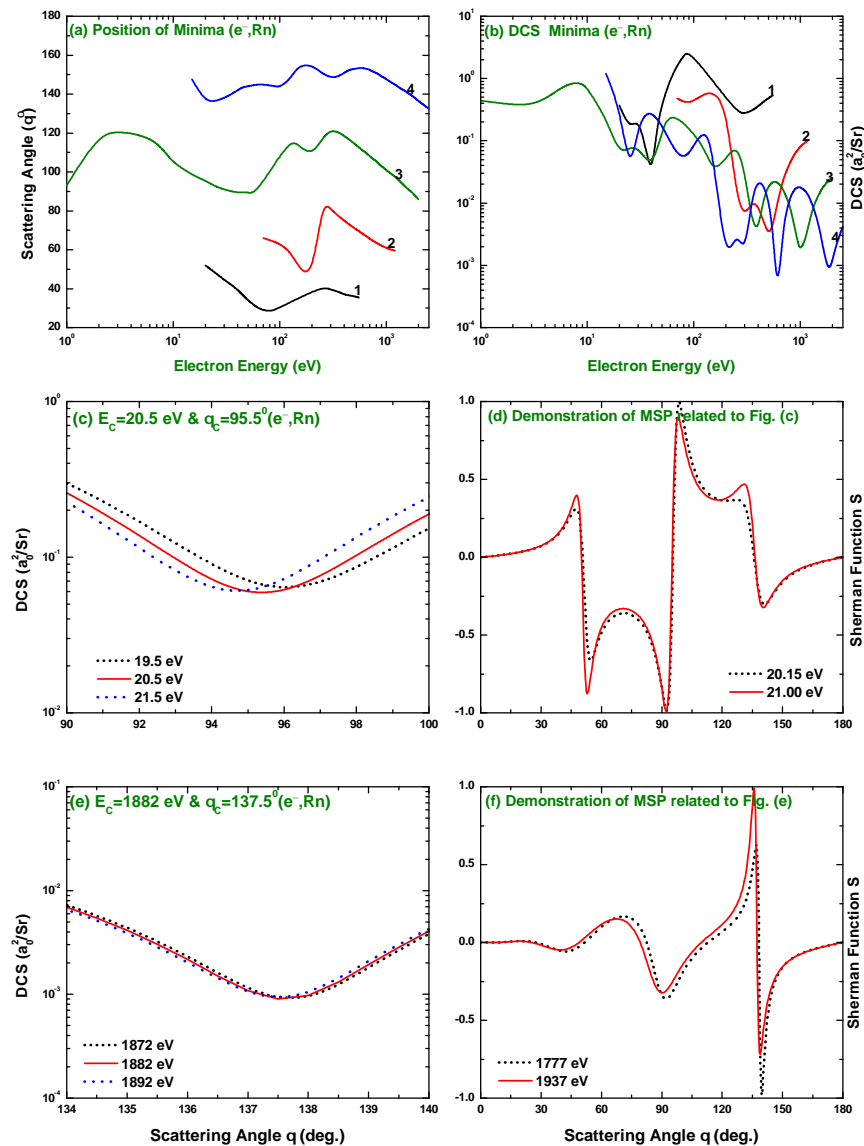


Figure 14. Energy dependence of the spin polarization parameters  $U$  and  $T$  for elastic scattering of electrons from neutral radon atoms at scattering angles (a,b):  $30^\circ$ , (c,d):  $90^\circ$  and (e,f):  $150^\circ$ .



As no experimental data and other theoretical studies of  $U$  and  $T$  parameters are available in the literature, we display only our present results providing further impetus for experimental data for anticipated applications. The spin asymmetry parameters  $S(\theta)$ ,  $U(\theta)$  and  $T(\theta)$  arise from the interference effect of the direct and spin-flip amplitudes and they are sensitive to both the spin-dependent and correlation interactions. The values of  $U$  and  $T$  depend on  $S$  by the conservation relation:  $S^2 + U^2 + T^2 = 1$ , and are useful indicators of the total polarization,  $S(\theta) = \pm 1$ .

In Figure 15a, we display the energy dependence of the angular distribution of the DCS minima obtained for electrons elastically scattered from neutral radon atoms. As seen in this figure, the low-angle minima, corresponding to curves 1 and 2, are not found in the DCSs below 11 eV, but maintain their appearance up to 1200 eV. The angular positions of these minima vary from  $28^\circ$  at 75 eV to  $83^\circ$  at 300 eV. The intermediate-angle minima (curve 3), on the other hand, are present at all energies below 2000 eV with the angular positions varying between  $88^\circ$  and  $120^\circ$ . The high-angle minima (curve 4) in the DCS are seen to appear for collision energies  $10.8 \leq E_i \leq 2500$  eV.



**Figure 15.** Energy dependence of the angular positions (a) and the DCS values (b) of the deep minima for electrons elastically scattered from neutral radon atoms. Furthermore, are presented the angular dependence of the DCS and  $S(\theta)$  for some incident energies in the vicinity of the critical minimum at ( $E_c=20.5$  eV,  $\theta_c = 95.5^\circ$ ) (c,d) and ( $E_c=1882$  eV,  $\theta_c = 137.5^\circ$ ) (e,f).

There are some deep minima which remain conspicuous among the minimal DCS values. Furthermore, these deepest minima can be traced by plotting the energy dependent angular distribution of the DCS minima, shown in Figure 15a. The present study predicts a total of 18 deep minima in the DCS, those are depicted in Figure 15b. There are 6 such deep minima from each of the low-angle (curves 1 and 2), intermediate-angle (curve 3) and high-angle (curve 4) regions. The low-angle minima are visible at 22.8, 39.2, 100, 284.0, 300 and 502.75 eV; the intermediate-angle minimum are at 2.5, 20.5, 38.6, 180, 381.0 and 1004.5 eV; and the high-angle minimum are at 24.8, 80, 199.0, 289.5, 608.0 and 1882.0 eV. For these energy-dependent DCS deep minima to be a critical minimum (CM), there are three important criteria: (i) the magnitude of the spin-flip amplitude must be larger than that of the direct amplitude, i.e.,  $|g(\theta)| > |f(\theta)|$ , (ii) the DCS at a CM attains a local minimum, and (iii) in the vicinity of a CM, the scattered electrons acquire total polarization ( $S = \pm 1$ ).

In view of criterion (i), among the 18 deep minima, shown in Figure 15b, 14 deep minima qualify to be CM. The remaining 4 minima, located at 80, 100, 180 and 300 eV, are not CM as  $|g(\theta)| < |f(\theta)|$  for them. The energy and angular positions of the 14 CMs, denoted, respectively, by the critical energies  $E_c$  and the critical angles  $\theta_c$ , are listed in Table 1. The positions of these CMs in terms of impact energy as well as scattering angle are clearly shown in 3D-plot of the DCS in Figure 16. The highest critical energy ( $E_c = 1882.0$  eV) occurs at  $\theta_c = 137.5^\circ$  whereas the highest critical angle ( $\theta_c = 155.0^\circ$ ) shows up at  $E_c = 199.0$  eV.

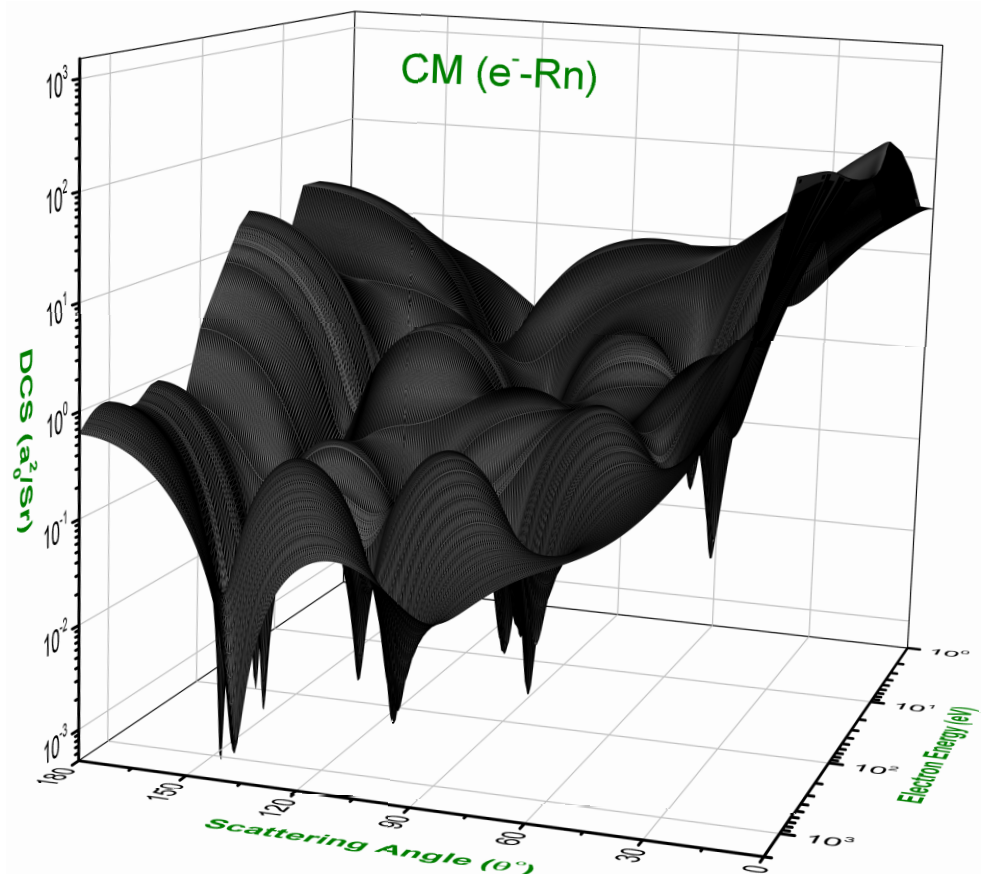


**Figure 16.** A three dimensional plot of the present DCS for electrons elastically scattered from neutral radon atoms.

**Table 1.** The positions of the DCS CM predicted by the present theory for electrons elastically scattered from neutral radon atoms.

$E_c$   (eV)	$\theta_c$ (deg.)	$ f(\theta) $ (cm)	$ g(\theta) $ (cm)
2.5	120.5	$1.92 \times 10^{-9}$	$3.90 \times 10^{-9}$
20.5	95.5	$3.73 \times 10^{-10}$	$1.46 \times 10^{-9}$
22.8	49.5	$1.66 \times 10^{-10}$	$2.06 \times 10^{-9}$
24.8	136.5	$1.89 \times 10^{-10}$	$9.11 \times 10^{-10}$
38.6	90.0	$2.04 \times 10^{-10}$	$1.10 \times 10^{-9}$
39.2	39.5	$2.59 \times 10^{-10}$	$8.38 \times 10^{-10}$
199.0	155.0	$7.92 \times 10^{-11}$	$1.90 \times 10^{-10}$
284.0	82.0	$6.46 \times 10^{-11}$	$3.76 \times 10^{-10}$
289.5	149.0	$1.42 \times 10^{-11}$	$1.73 \times 10^{-10}$
381.0	119.5	$8.37 \times 10^{-11}$	$3.05 \times 10^{-10}$
502.75	71.0	$1.30 \times 10^{-11}$	$3.35 \times 10^{-10}$
608.0	153.5	$6.49 \times 10^{-11}$	$9.92 \times 10^{-11}$
1004.5	101.0	$1.44 \times 10^{-11}$	$3.05 \times 10^{-10}$
1882.0	137.5	$3.45 \times 10^{-11}$	$1.94 \times 10^{-10}$

In Figure 15c–f, also we consider our predicted CMs for criteria by presenting angular variations of DCS and Sherman function for some incident energies in the vicinity of two CMs at ( $E_c = 20.5$  eV;  $\theta_c = 95.5^\circ$ ) and (1882.0 eV, 137.5°). As evident in Figure 15c, the DCS attains its lowest value exactly at  $E_c = 20.5$  eV. A slight increase in energy to 21.5 eV or decrease to 19.5 eV, the DCS gets higher value. Similar result is also observed in Figure 15e, where the DCS value is lowest at  $E_c = 1882.0$  eV than the values at 1892.0 and 1872.0 eV in the proximity. Again, from Figure 15d, it follows that, in the vicinity of the CM at ( $E_c = 20.5$  eV;  $\theta_c = 95.5^\circ$ ), the maximum spin polarization (MSP) varies from  $-0.990$  at ( $E_i = 21$  eV;  $\theta = 92.0^\circ$ ) to  $+0.999$  at ( $E_i = 20.15$  eV;  $\theta = 98.5^\circ$ ). A similar behavior is also observed in Figure 15f for the CM at ( $E_c = 1882.0$  eV;  $\theta_c = 137.5^\circ$ ). Here, the MSP attains to  $+0.989$  and  $-0.982$  at ( $E_c = 1937.0$  eV;  $\theta_c = 136.0^\circ$ ) and ( $E_c = 1777.0$  eV;  $\theta_c = 139.5^\circ$ ), respectively, from positive and negative excursion. In the vicinity of each of 14 CMs, we have calculated MSP points at which the polarization reaches extremal values of both signs. A total of 28 such points are found and are listed in Table 2 with their energy  $E_d$  and angular  $\theta_d$  positions. One can see in Table 2 that a large polarization is achieved at all of these points that can be considered as total polarization points [41]. Figure 17 displays a 3D plot of the positions of these MSP points. All these results demonstrate the efficacy of the present theory in determining the CM positions precisely.

Table 2 also presents the energy widths  $\Delta E$ , the difference between  $E_c$  and  $E_d$ , and the angular widths  $\Delta\theta$ , the difference between  $\theta_c$  and  $\theta_d$ , for each MSP point. The evaluation of these energy and angular widths are important to know the sharpness of the DCS and corresponding  $S$  distribution at a CM. For an example, if we consider the high-angle CM at ( $E_c = 608.0$  eV,  $\theta_c = 153.5^\circ$ ), the corresponding MSP =  $+0.98937$  at  $E_d = 612.7$  eV with  $+\Delta E = |608.0 - 612.7| = 4.7$  eV and  $+\Delta\theta = |153.5 - 153.0| = 0.0^\circ$ , while MSP =  $-0.91133$  at  $E_d = 610.7$  eV with  $-\Delta E = |608.0 - 610.7| = 2.7$  eV and  $-\Delta\theta = |153.5 - 153.0| = 0.5^\circ$ . Therefore, the widths of the DCS valley are  $4.7 + 2.7 = 7.4$  eV along the energy axis and  $0.0^\circ + 0.5^\circ = 0.5^\circ$  along the angular axis. These widths indicate that the angular DCS distribution at the CM and the corresponding  $S$  distribution near the MSP points are both very sharp.

**Table 2.** Maximum spin polarization (MSP) with their positions ( $E_d, \theta_d$ ) and deviations in energy  $\Delta E$  and angle  $\Delta\theta$  from the respective CM positions for  $e^- - {}^{222}\text{Rn}$  elastic scattering.

MSP	$E_d$ (eV)	$\theta_d$ (deg)	$\pm\Delta E$ (eV)	$\pm\Delta\theta$ (deg)
+0.99912	2.90	116.5	0.40	4.0
-0.83577	4.95	124.0	2.45	3.5
+0.99897	20.15	98.5	0.35	3.0
-0.98950	21.00	92.0	0.50	3.5
+0.99888	24.10	47.5	1.30	2.0
-0.99728	21.70	52.0	1.10	2.5
+0.99172	23.70	134.5	1.10	2.0
-0.99993	25.60	137.5	0.80	1.0
+0.99863	40.60	87.0	2.00	3.0
-0.97013	34.00	92.0	4.60	2.0
+0.99630	36.70	41.0	2.50	1.5
-0.99872	40.70	38.5	1.50	1.0
+0.97862	192.00	156.0	7.00	1.0
-0.99858	201.50	154.5	2.50	0.5
+0.91586	266.00	82.5	18.00	0.5
-0.99647	299.00	82.0	15.00	0.0
+0.99018	291.50	148.0	2.00	1.0
-0.96734	276.20	150.0	13.30	1.0
+0.99993	360.00	121.0	21.00	1.5
-0.99981	401.00	118.0	20.00	1.5
+0.97688	486.00	70.5	16.75	0.5
-0.93089	517.50	71.5	14.75	0.5
+0.98937	612.70	153.5	4.70	0.0
-0.91133	610.70	153.0	2.70	0.5
+0.99497	1002.00	99.5	2.50	1.5
-0.95727	1004.00	102.5	0.50	1.5
+0.98881	1937.0	136.0	55.00	1.5
-0.98166	1777.0	139.5	105.0	2.0

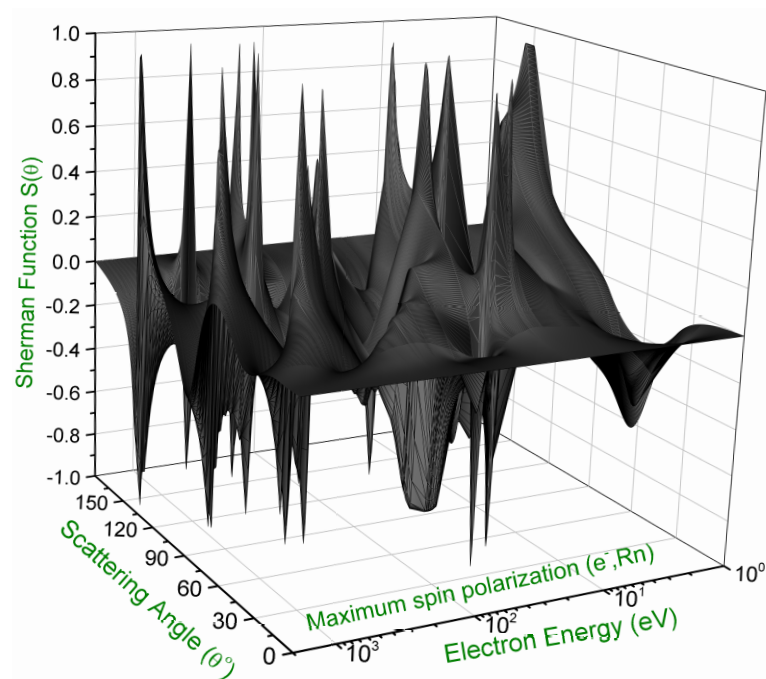


**Figure 17.** A 3D-plot of the present Sherman function for electrons elastically scattered from neutral radon atoms.

In Figure 18, we present our results of the integrated elastic (IECS), momentum-transfer (MTCS), viscosity (VCS), inelastic (INCS) and total (TCS) cross sections for  $1 \text{ eV} \leq E_i \leq 100 \text{ keV}$  electrons scattering from neutral radon atoms. We are not aware of any experimental data of these observables available in the literature. Therefore, we compare our results of IECS, MTCS, INCS and TCS with theoretical predictions of Neerja et al. [19] available at  $E_i = 2.0\text{--}500.00 \text{ eV}$  and IECS, MTCS and VCS of Mayol and Salvat [20] at  $E_i = 100 \text{ eV}\text{--}100 \text{ keV}$ . The comparison shows that our results agree well with those of Mayol and Salvat [20]. At  $E_i < 100 \text{ eV}$ , our results disagree significantly with those of Neerja et al. [19] specially in the vicinity of minima positions. In this energy domain, the present theory predicts deep minima whereas the predictions from [19] show very shallow minima. One can see that, beyond  $5 \text{ eV}$  (the first excitation energy of radon), the TCS is greater than IECS. This is expected because of the absorption of some particles into the inelastic channels.

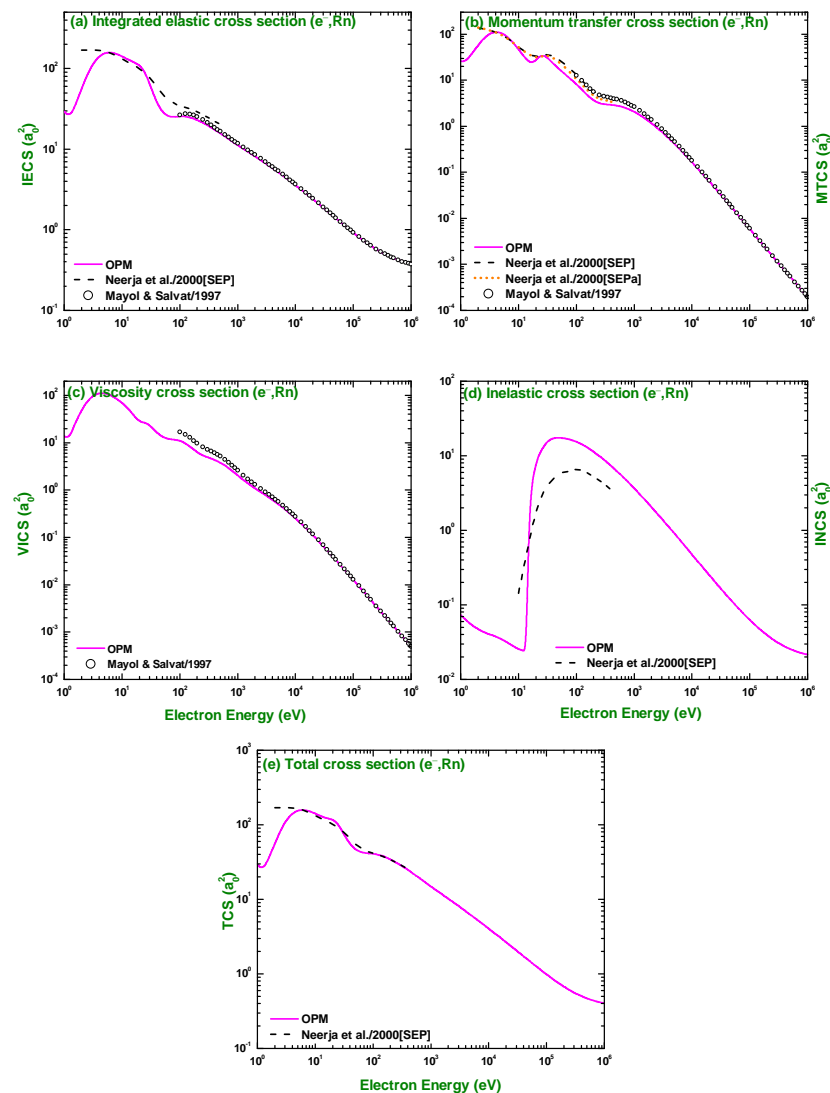


**Figure 18.** Energy dependence of the (a) integrated elastic, (b) momentum-transfer, (c) viscosity, (d) inelastic and (e) total cross sections for electron impact scattering from neutral radon atoms. Presented are the theoretical calculations — for the present results, — — — for Neerja et al. [19], .... for Neerja et al. [19] and ○ ○ ○ for Mayol and Salvat. SEP and SEPa, respectively, denote the static-exchange-polarization potentials and SEP with absorption potential.

#### 4.2. Positron Scattering from Neutral Radon

Figures 19–22 present angular dependent DCS for the elastic scattering of positrons from neutral radon at impact energies  $10 \text{ eV} \leq E_i \leq 10 \text{ keV}$ . As evident in these figures, unlike electron DCSs the positron counterparts show relatively fewer number of maxima and minima. Two significant minima are seen at  $E_i = 10 \text{ eV}$  and only one at  $10 < E_i \leq 30 \text{ eV}$ . After that few very shallow minima are obtained within the energy domain of  $40 \text{ eV} \leq E_i \leq 150 \text{ eV}$  confined to lower scattering angles. At 200 eV and beyond, the DCS values decrease monotonously with increasing incident energies.

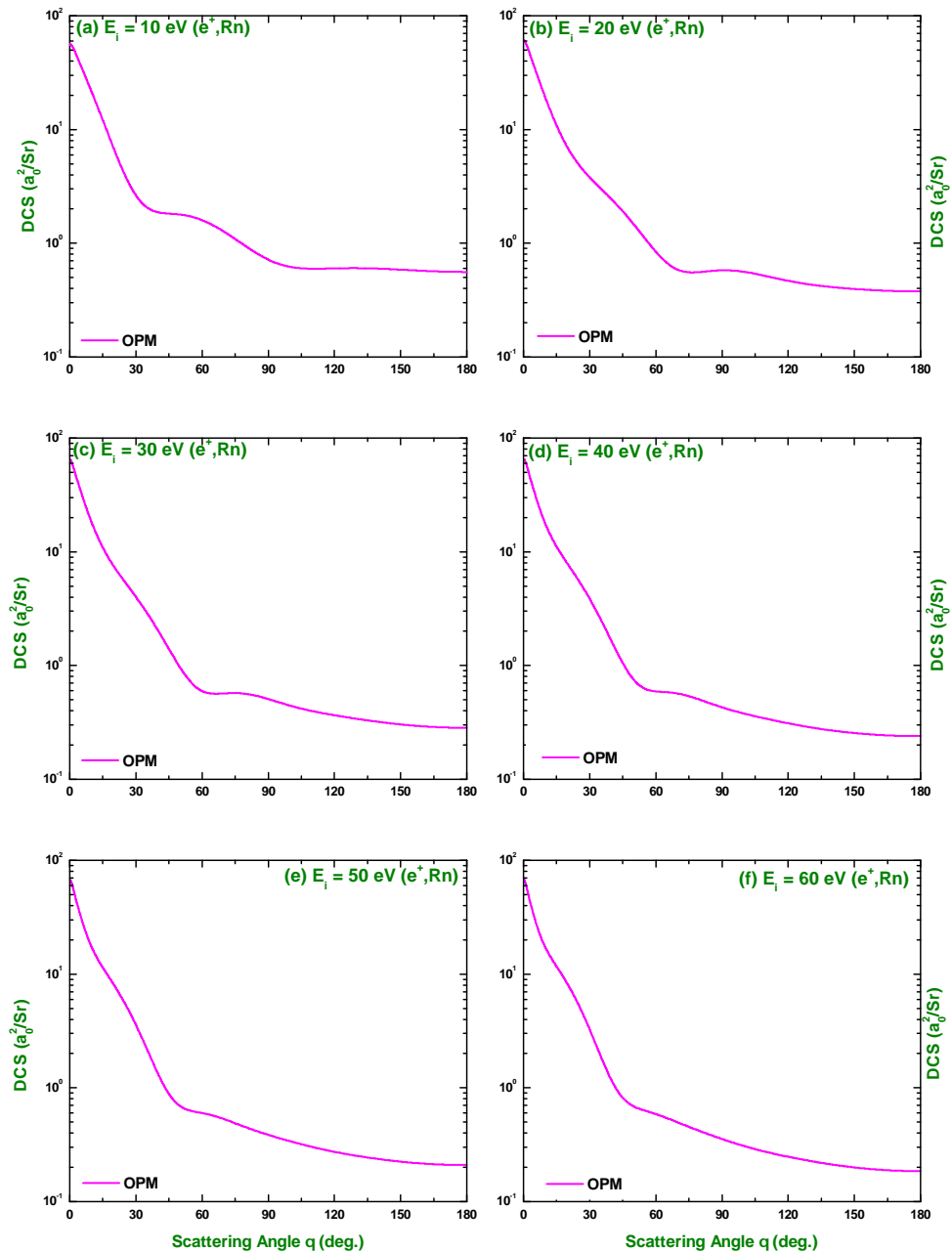


Figure 19. Differential cross sections for 10, 20, 30, 40, 50 and 60 eV positrons elastically scattered from neutral radon atoms as a function of scattering angle.

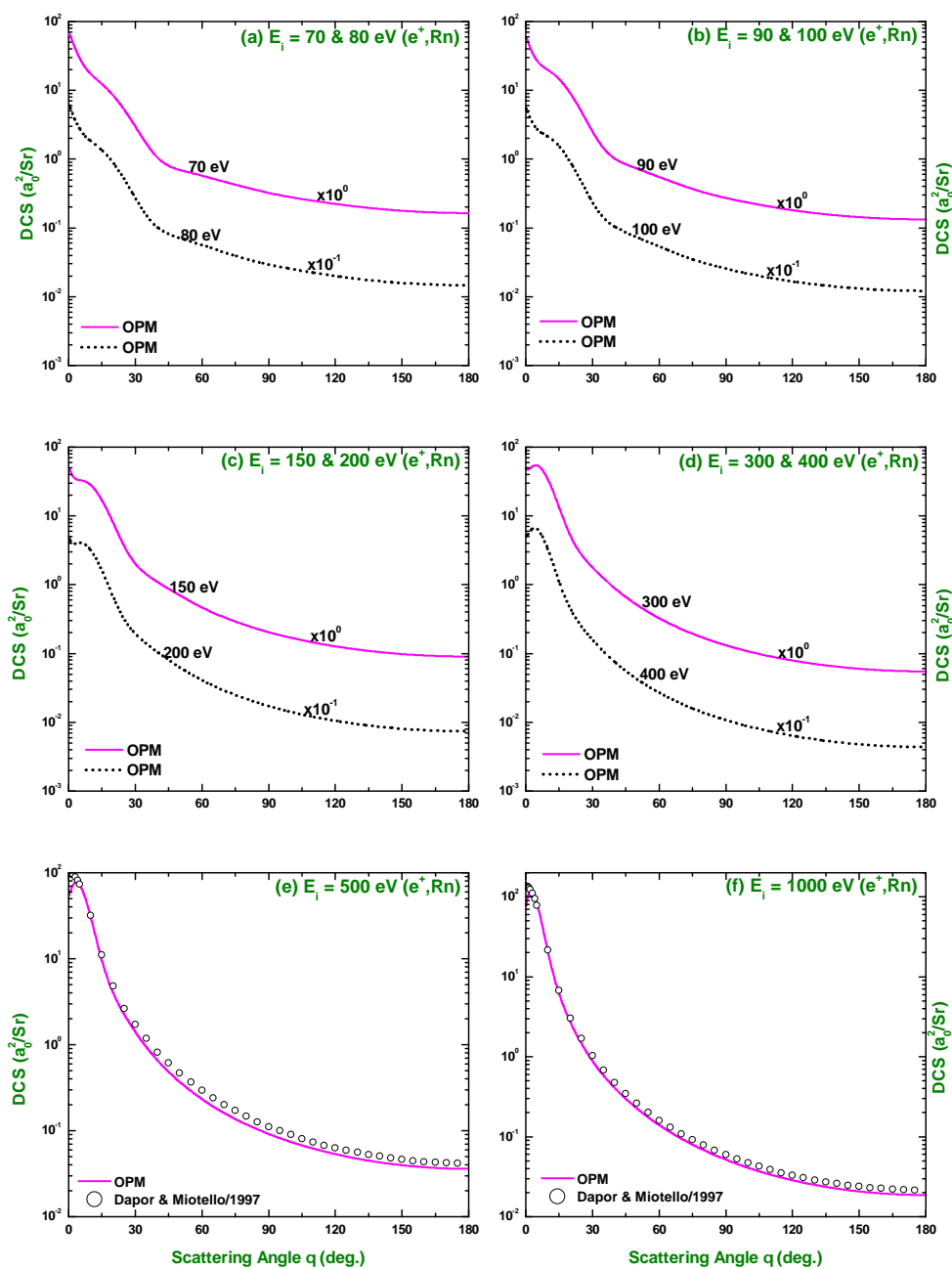
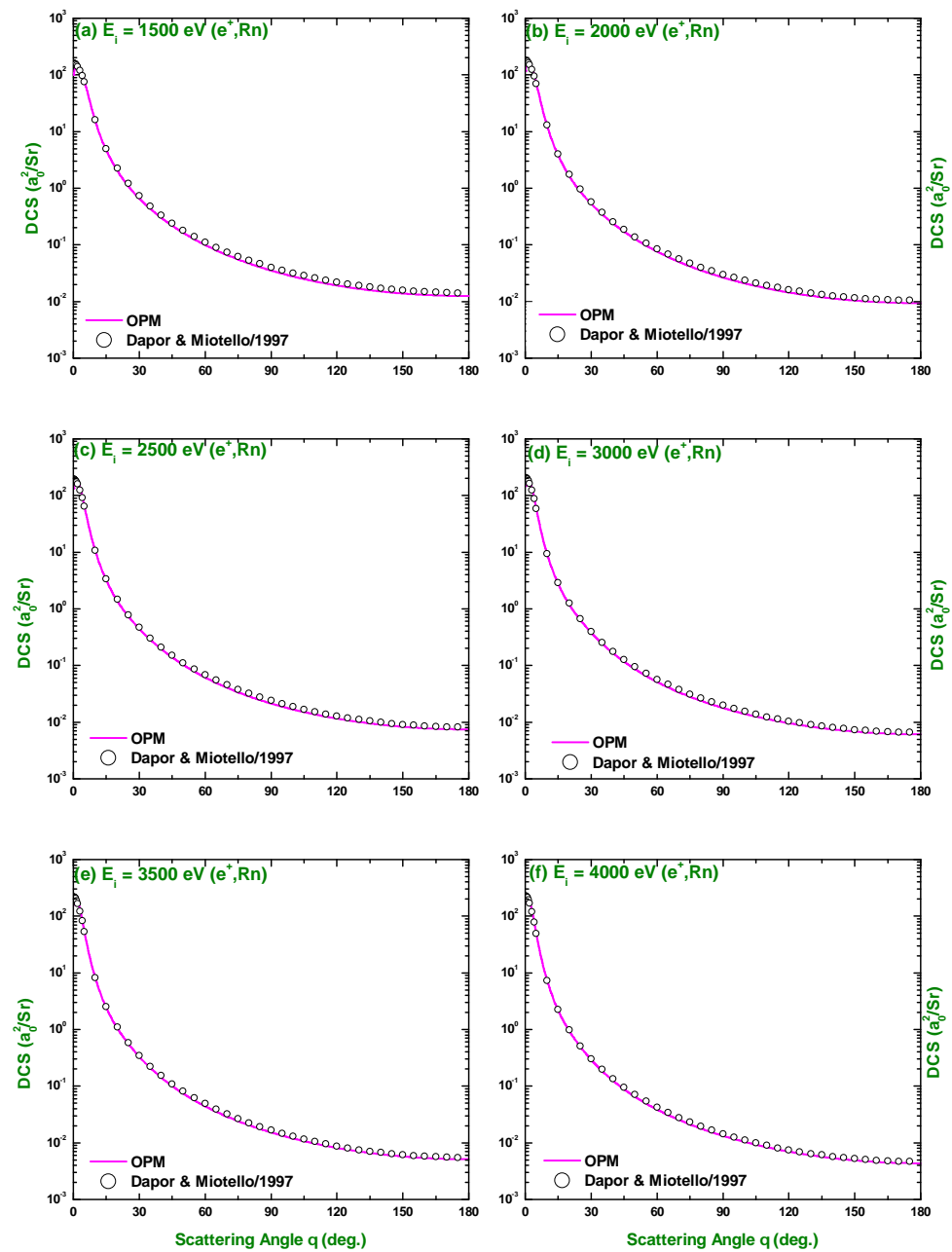


Figure 20. Same as Figure 19, but at impact energies of (a) 70 and 80 eV, (b) 90 and 100 eV, (c) 150 and 200 eV, (d) 300 and 400 eV, (e) 500 eV, and (f) 1000 eV. In addition, the calculations of Dapor and Miotello [21] at 500 and 1000 eV are presented.





**Figure 21.** Same as Figure 19, but at impact energies of 1500, 2000, 2500, 3000, 3500 and 4000 eV.  $\circ \circ \circ$  curves are the calculations of Dapor and Miotello [21].

We have not found any experimental measurements for positron impact on radon targets. The present DCS results for positron impact scattering are, therefore, compared with the only calculations of Dapor and Miotello [21] available for  $E_i = 500\text{--}4000$  eV. The comparison shows that the two calculations agree very well with each other except a slight differences in magnitude at 500 eV for higher scattering angles.

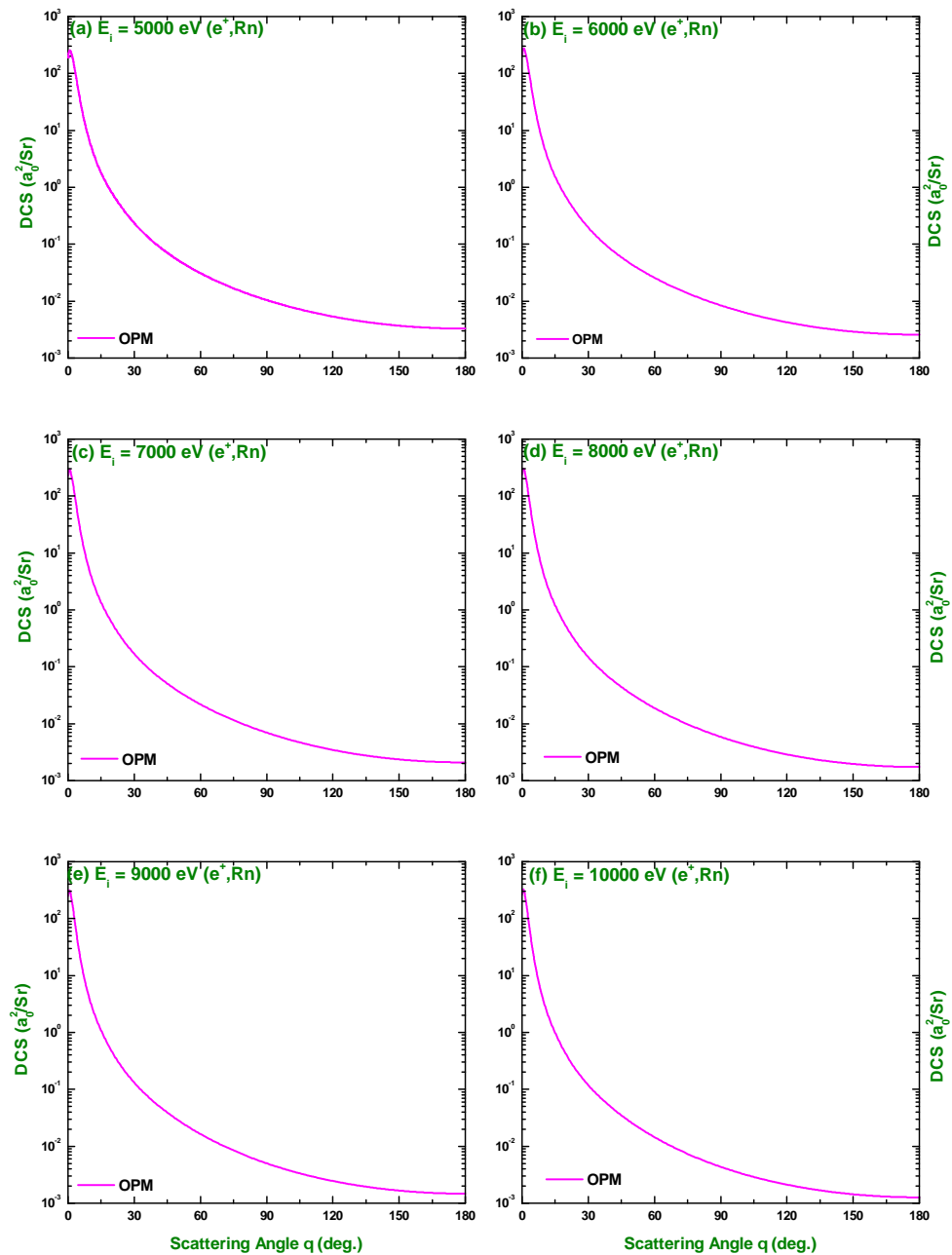
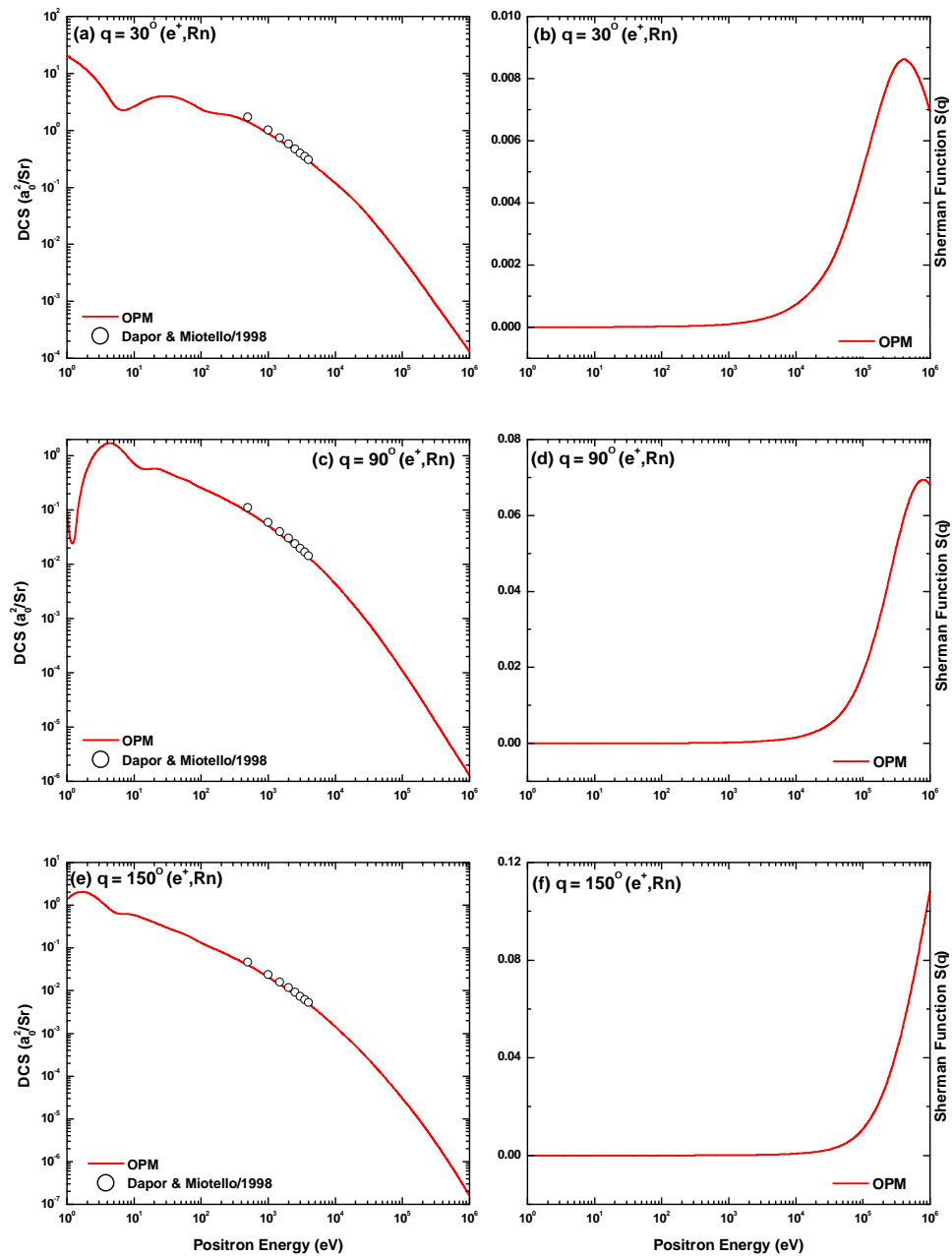


Figure 22. Same as Figure 19, but at impact energies of 5, 6, 7, 8, 9 and 10 keV.

In Figure 23, we display energy dependence of the DCS and of the corresponding Sherman function for positron scattering from neutral radon atoms at three scattering angles  $30^\circ$ ,  $90^\circ$  and  $150^\circ$ . As seen in this figure, minor structures appear in the DCS distributions at lower scattering angles, and they fade with the increase of energy. The present DCSs are again compared with those of Dapor and Miotello [21]. Similar to the case of electron scattering, the Sherman function increases with increasing scattering angles. However, the positron spin polarization is considerably smaller than that of its electron counterpart. This might be due to the Coulomb-dominated behavior of the positron potential [42].



**Figure 23.** Energy dependence of the DCS and the Sherman function for positrons elastically scattered from neutral radon atoms at scattering angles (a,b): 30°, (c,d): 90° and (e,f): 150°.

Energy dependence of the spin polarization parameters  $U$  and  $T$  for positrons elastically scattered from neutral radon atoms are depicted in Figure 24 at  $\theta = 30^\circ, 90^\circ$  and  $150^\circ$ . It is observed in this figure that, as expected, the variation of  $U$  and  $T$  with energy are opposite to each other. Starting from zero, the magnitude of  $|U(\theta)|$  increases very slowly up to  $E_i = 10$  keV, and beyond that it increases rapidly and reaches its maximum value. The maximum value of  $|U(\theta)|$  is obtained at  $\theta = 90^\circ$ . Below and beyond this scattering angle, the  $|U(\theta)|$  values decrease. The parameter  $T$ , on the other hand, starts at its maximum and slowly decreases with energies. Beyond  $E_i = 10$  keV, the values of  $|T(\theta)|$  sharply fall to its minimum, which is the lowest at  $\theta = 90^\circ$ . We are not aware of any experimental or any other theoretical studies regarding these parameter for  $e^\pm - \text{Rn}$  scattering. We expect that the present study will encourage both experimental and theoretical groups to pay their attention to this scattering system.

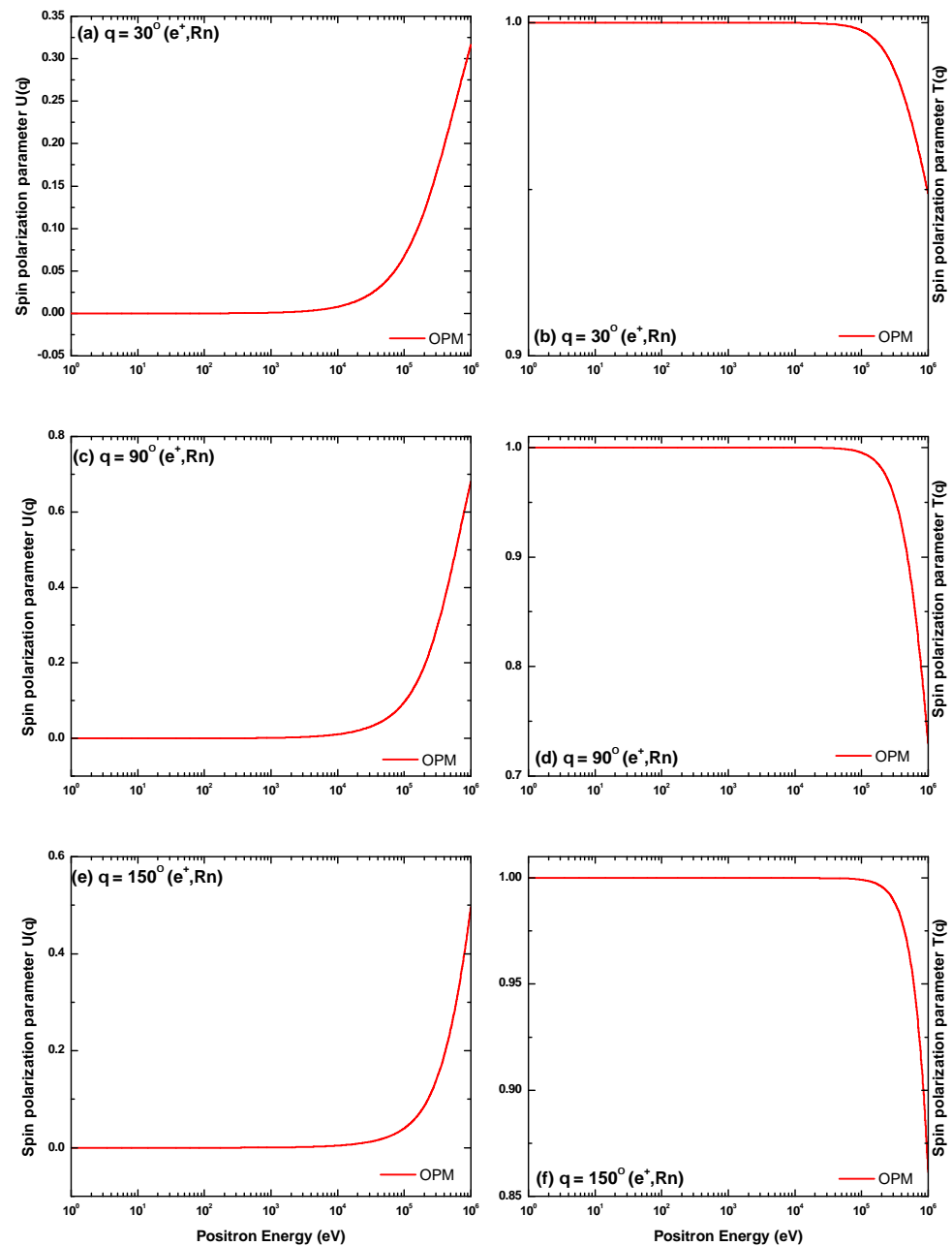


**Figure 24.** Energy dependence of the spin polarization parameters  $U$  and  $T$  for positrons elastically scattered from neutral radon atoms at scattering angles (a,b):  $30^\circ$ , (c,d):  $90^\circ$  and (e,f):  $150^\circ$ .

For  $e^+_{-222}\text{Rn}$  scattering, the present results of IECS, MTCS, VCS, INCS and TCS calculated for  $1 \text{ eV} \leq E_i \leq 1 \text{ MeV}$  are presented in Figure 25. It is noticeable that all these results are considerably different in values and shape from their electron counterparts. The magnitude of these cross sections is two to three times smaller than those due to electron scattering. Regarding the shape, on the other hand, some structures are clearly visible in IECS, MTCS and VCS curves for electron scattering, whereas they are very shallow in the case of positron scattering. These variations certainly support the fact that the  $e^+_{-222}\text{Rn}$  interaction is rather weaker as compared to its electron counterpart. It is worth mentioning that the interaction potentials involved in these two projectiles are drastically different. In the case of positron projectile, the static potential ( $V_{st}$ ) is repulsive and the exchange potential ( $V_{ex}$ ) is absent as opposed to the electron projectile. Moreover, the polarization potential of the short range parts also different for both the projectiles.

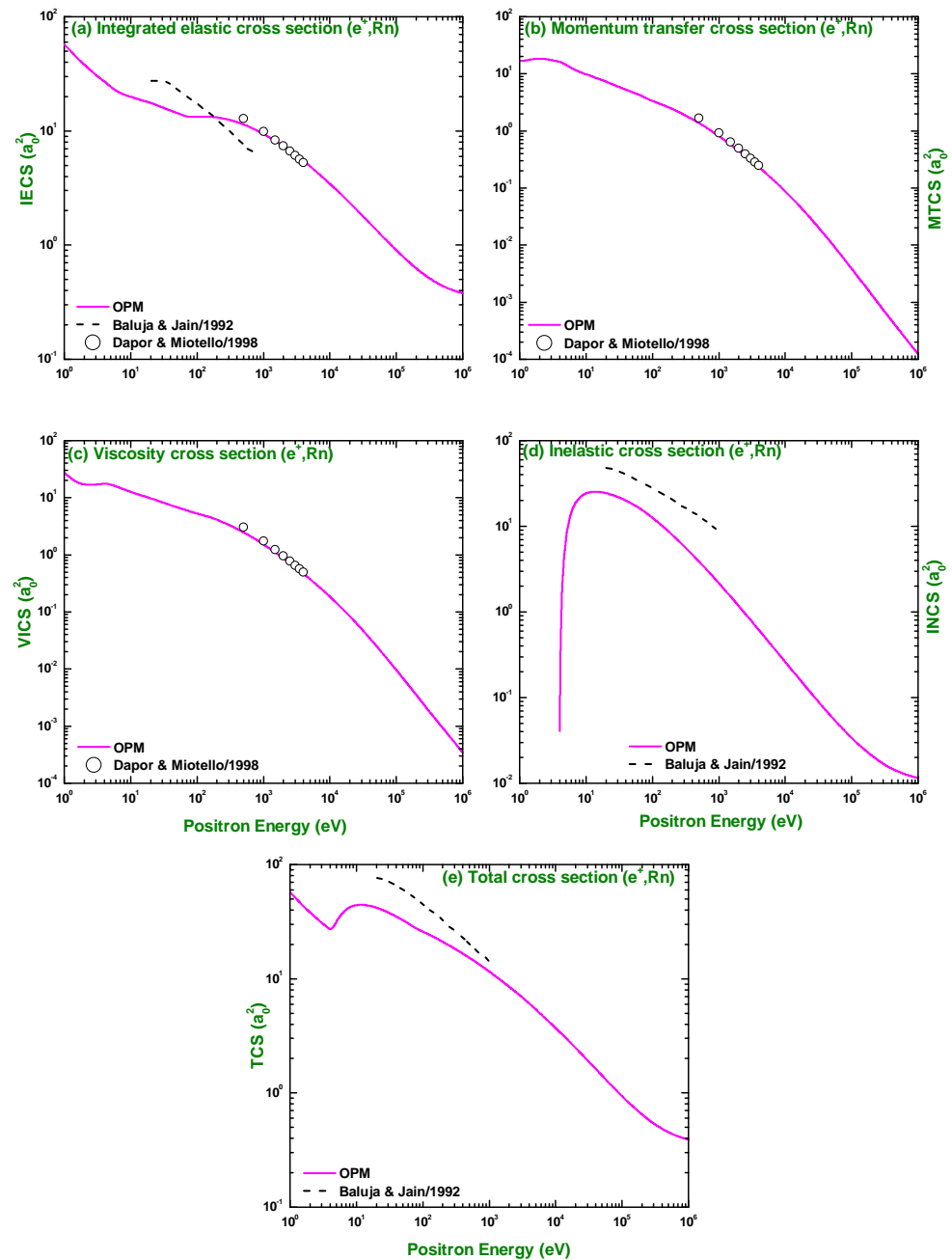


**Figure 25.** Energy dependence of the (a) integrated elastic, (b) momentum-transfer, (c) viscosity, (d) inelastic and (e) total cross sections for positron impact scattering from neutral radon atoms. Presented are the theoretical calculations — for the present results, — — for Baluja and Jain [12] and  $\circ \circ \circ$  for Dapor and Miotello [21].

Because of the absence of any experimental data of the above scattering observables we compare our IECS, INCS and TCS results with the theoretical calculations of Baluja and Jain [12] available for  $20 \text{ eV} \leq E_i \leq 1 \text{ keV}$  and our IECS, MTCS and VCS results with those of Dapor and Miotello [21] available for  $0.5 \text{ keV} \leq E_i \leq 4 \text{ keV}$ . The comparison shows that the present results produce a nice agreement with those of Dapor and Miotello [21]. However, a noticeable disagreement is seen between our results and those of Baluja and Jain [12], especially in the case of IECS. This difference again might be due to the different procedures of calculations used by these two methods.

4.3.  $e^\pm$  Scattering from Radon Ions

In Figures 26 and 27, the energy dependent DCS and the corresponding Sherman function for  $e^-$ - $Rn^{q+}$  scattering are displayed, where  $q = 1, 10, 30, 50, 70$  and  $86$  indicates the ionic states, at a fixed scattering angle of  $90^\circ$ . To the best of our knowledge, there are neither any experimental nor any other theoretical studies on these scattering systems available in the literature.

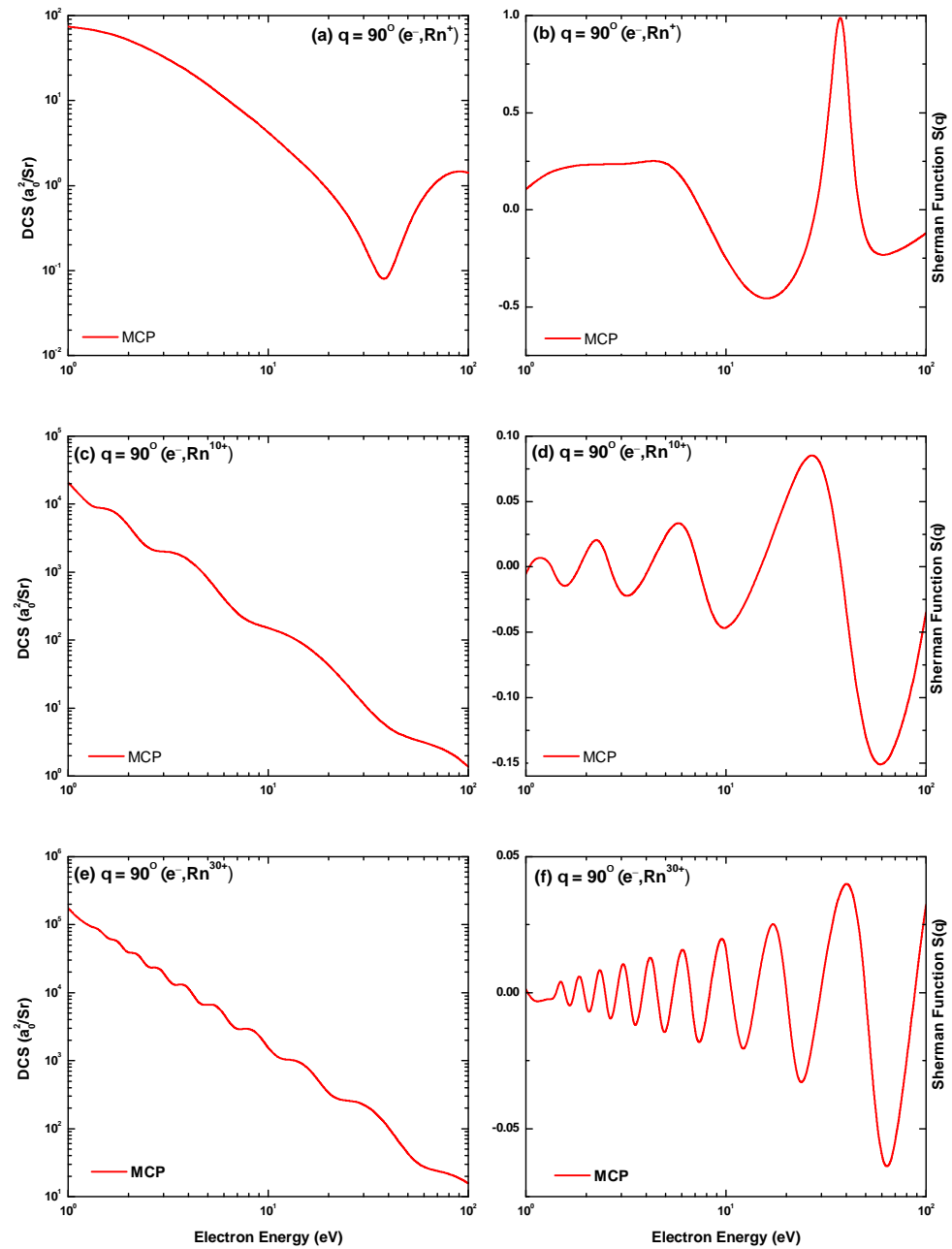
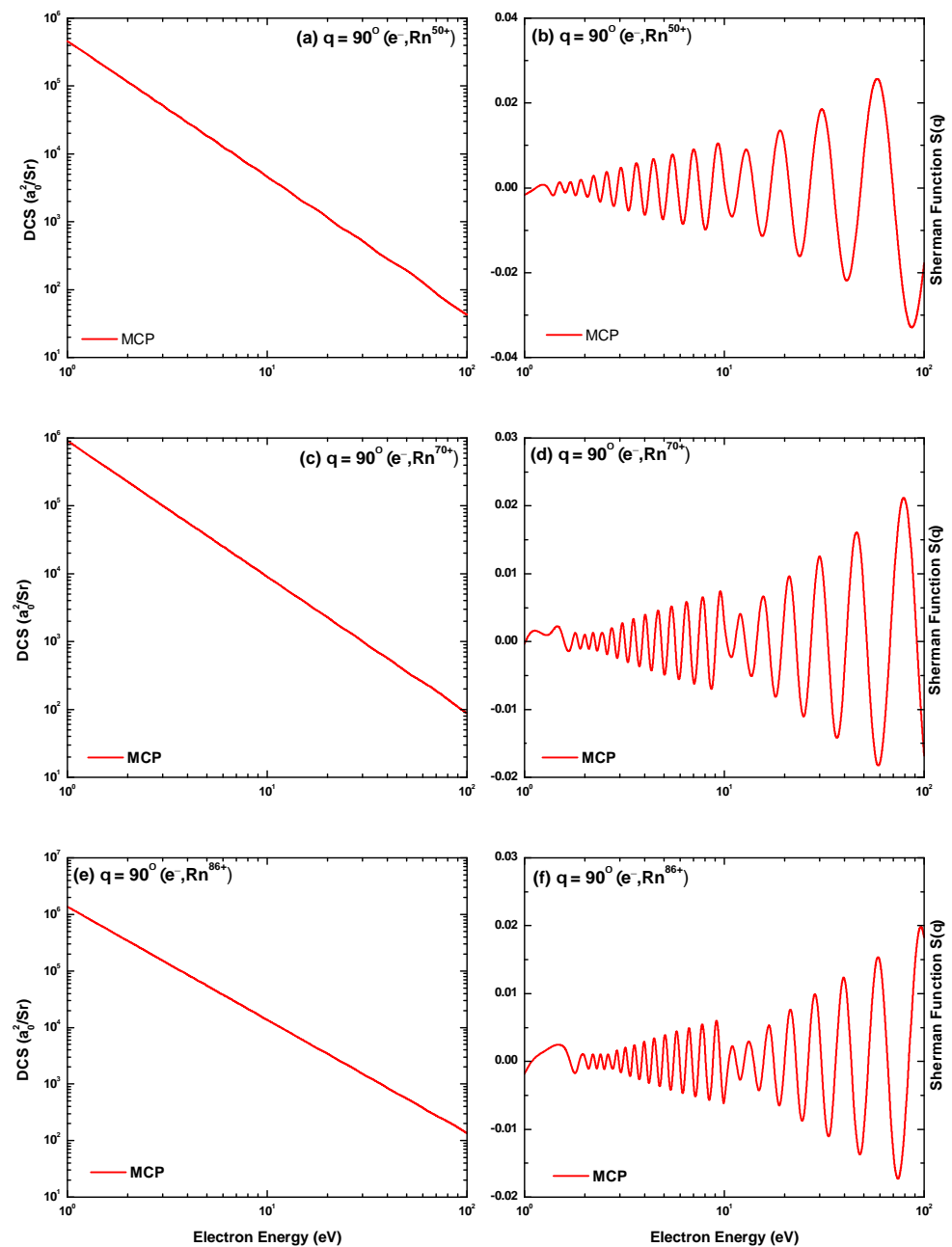


Figure 26. Energy dependent DCS and corresponding Sherman function for the elastic scattering of electrons from (a,b):  $Rn^+$ , (c,d):  $Rn^{10+}$  and (e,f):  $Rn^{30+}$  at fixed scattering angle  $\theta = 90^\circ$ .



**Figure 27.** Energy dependent DCS and corresponding Sherman function for the elastic scattering of electrons from (a,b):  $\text{Rn}^{50+}$ , (c,d):  $\text{Rn}^{70+}$  and (e,f):  $\text{Rn}^{86+}$  at fixed scattering angle  $\theta = 90^\circ$ .

As seen in Figures 26 and 27, the DCS values, at a particular energy, increase with increasing ionic charge of the target. This is expected according to the Rutherford scattering formula. The number of structures in DCSs increases with increasing ionic charge. However, increasing charge state weakens the interference pattern. This might be due to the decreasing contributions of short range potential of the bound electrons. Sharp structures in DCS are observed at low energies. This could be explained as the interference effect between the scattered waves due to the short range and Coulombic forces. At such low energies, velocity of the incident electron is comparable to the velocities of the bound electrons of the ion. Furthermore, the short range potential becomes important due to the enhanced electron-electron correlations. The structures in the Sherman function are related to those in the DCSs, but they are more pronounced in Sherman function distributions.

Figures 28 and 29 display the DCS and the corresponding Sherman function results for positron projectiles elastically scattered from various ionic states of radon. It is seen



that the variation of the cross section and the corresponding Sherman function with the ionic charge is similar to their electron counterpart. However, the spin asymmetry for positrons is extremely small signifying that the positron scattering is rather weaker than the electron scattering.

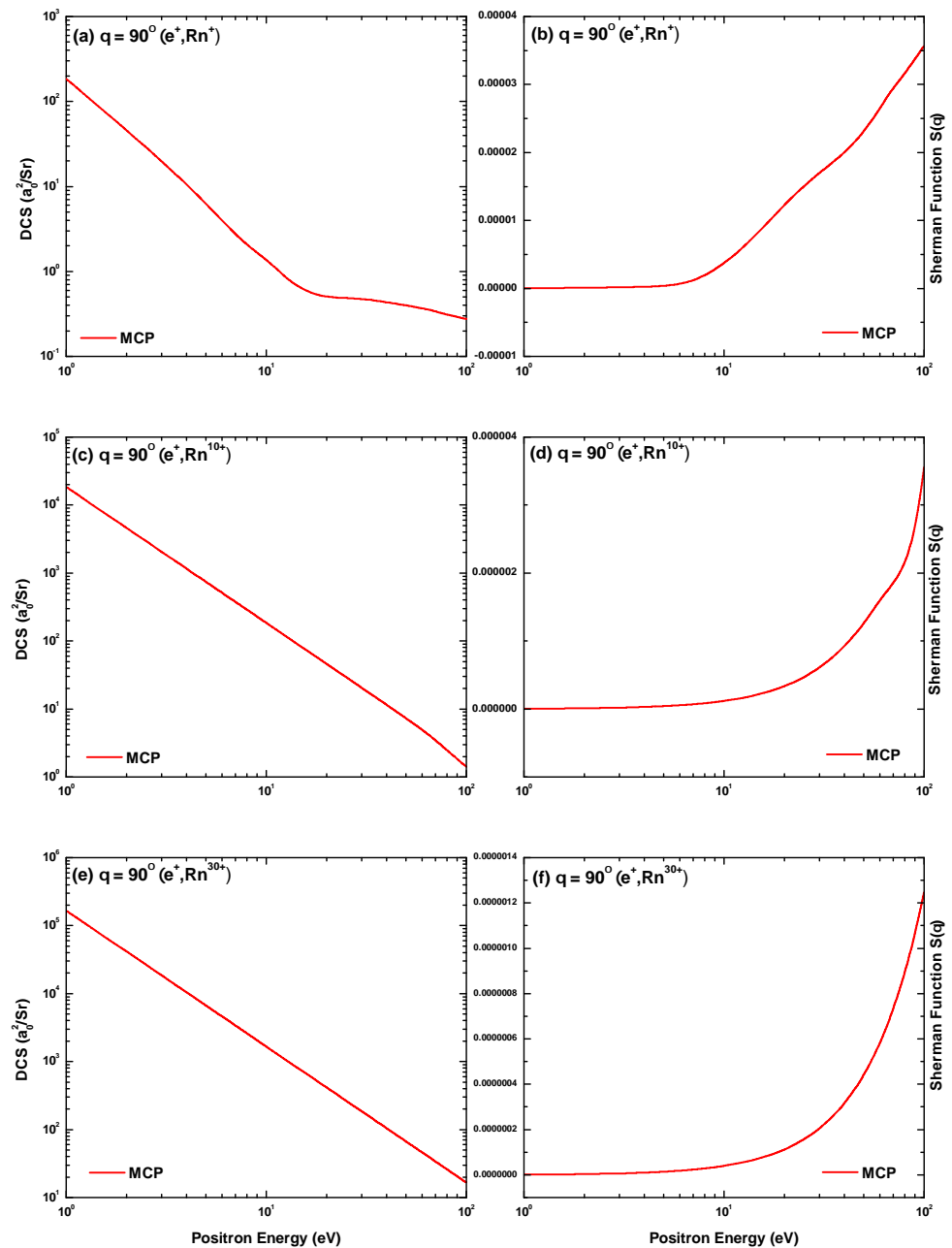
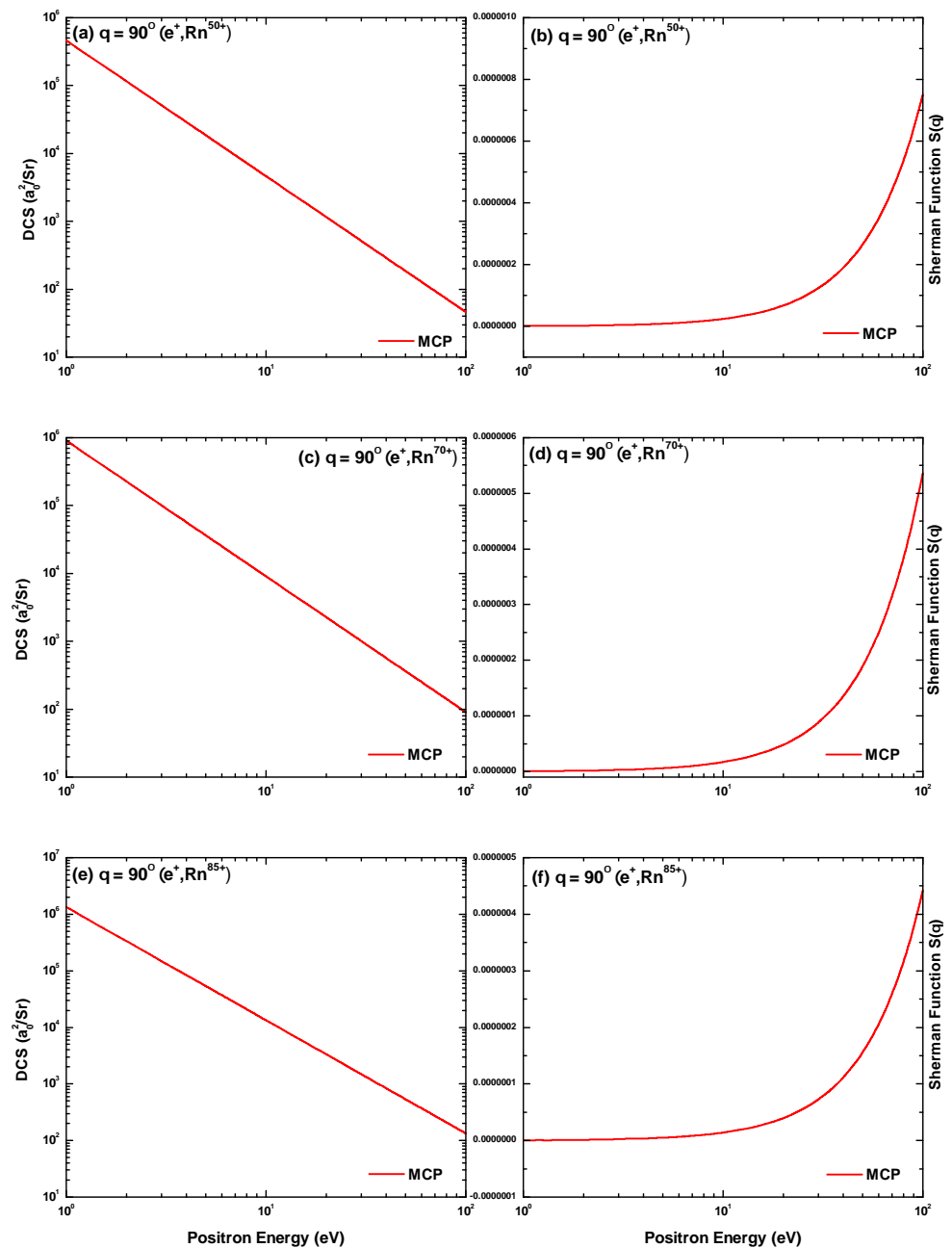
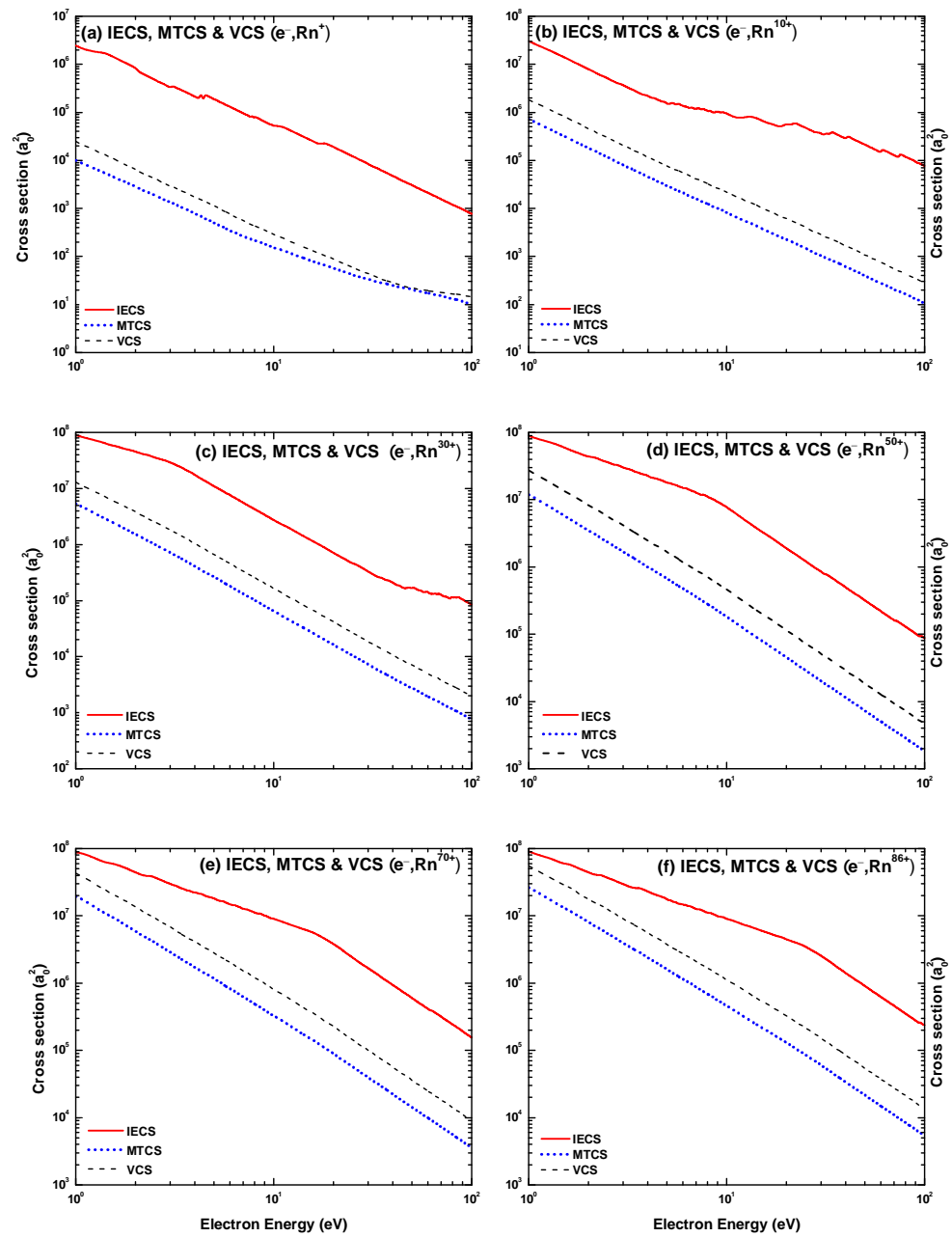


Figure 28. Energy dependent DCS and corresponding Sherman function for positrons elastically scattered from (a,b):  $Rn^+$ , (c,d):  $Rn^{10+}$  and (e,f):  $Rn^{30+}$  at fixed scattering angle  $\theta = 90^\circ$ .



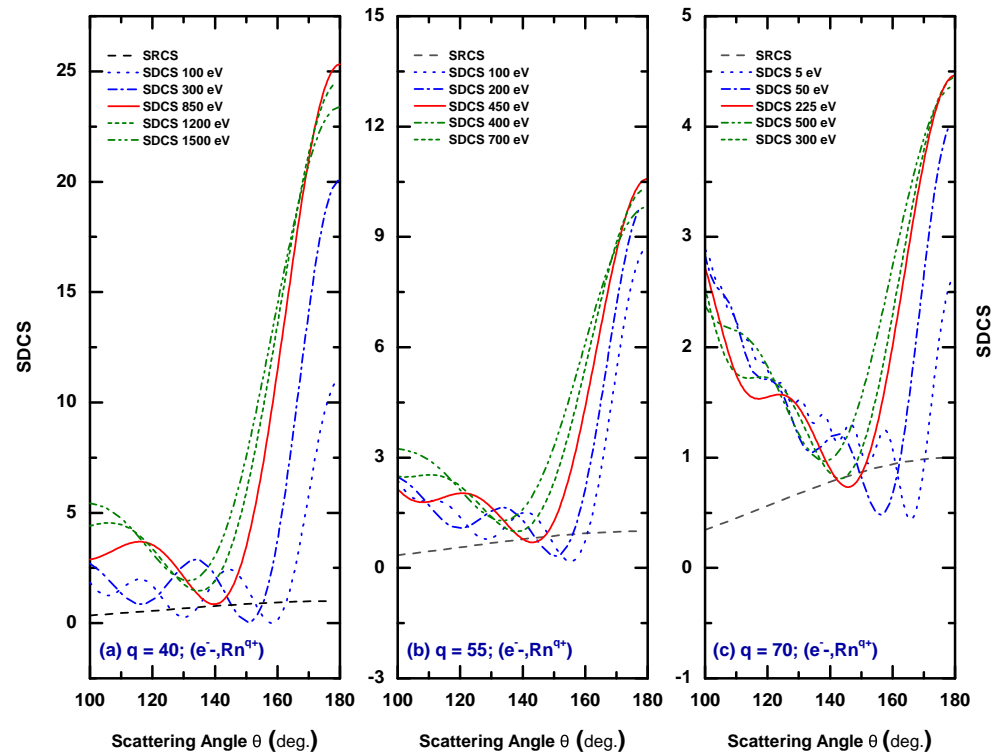
**Figure 29.** Energy dependent DCS and corresponding Sherman function for positrons elastically scattered from (a,b):  $\text{Rn}^{50+}$ , (c,d):  $\text{Rn}^{70+}$  and (e,f):  $\text{Rn}^{85+}$  at fixed scattering angle  $\theta = 90^\circ$ .

Figure 30 displays the energy variation of the IECS, MTCS and VCS of electrons elastically scattered from different charge states of radon ions. As seen in this figure, for ions with lower  $q$  ( $< 30$ ), the IECS increases with increasing the charge. This is expected because of the screening effect of the surrounding electron cloud. The interaction potential energy of the projectile electron with bound electron cloud is opposite in sign to that of the nucleus charge. Furthermore, the screening effect of the surrounding electron cloud is, therefore, strong for the ions of lower charge. The cross section increases as the increase of  $q$  diminishes the screening effect. It is also evident that, for ( $q \geq 30$ ), the IECS is almost independent of  $q$  and varies in conformity with the Rutherford scattering formula corresponding to the nuclear charge  $Z$ . For ions with higher  $q$ , the cross section is almost solely determined by the nuclear charge of the ion. From Figure 28, one can see the similar trend in the energy dependent MTCS and VCS with the ion charge  $q$ .



**Figure 30.** Energy dependence of the IECS, MTCS and VCS for the elastic scattering of electrons from (a)  $Rn^+$ , (b)  $Rn^{10+}$ , (c)  $Rn^{30+}$ , (d)  $Rn^{50+}$ , (e)  $Rn^{70+}$  and (f)  $Rn^{86+}$ .

Figure 31 presents the Coulomb glory at three different ionic states ( $q = 40, 55$  and  $70$ ) of radon. This Coulomb glory arises due to the electrostatic screening of nuclear potential by atomic electrons. Because of the presence of Coulomb glory the scaled differential cross section (SDCS) becomes maximum at  $\theta = 180^\circ$ . An important feature of the Coulomb glory is that for a particular ion charge, there is a critical energy at which the SDCS gets its maximum value. In the vicinity of that critical energy the cross sections become smaller. As seen in Figure 31a, for  $q = 40$ , the maximum SDCS is observed at  $E_i = 850$  eV. Furthermore, SDCS gets lower values both for increasing energy to 1200 eV or decreasing to 300 eV. Similar results are also observed for the ionicities  $q = 55$ , in Figure 31b, and for  $q = 70$ , in Figure 31c. The maximum SDCSs, for later two ionicities, are observed at  $E_i = 450$  and 225 eV, respectively.



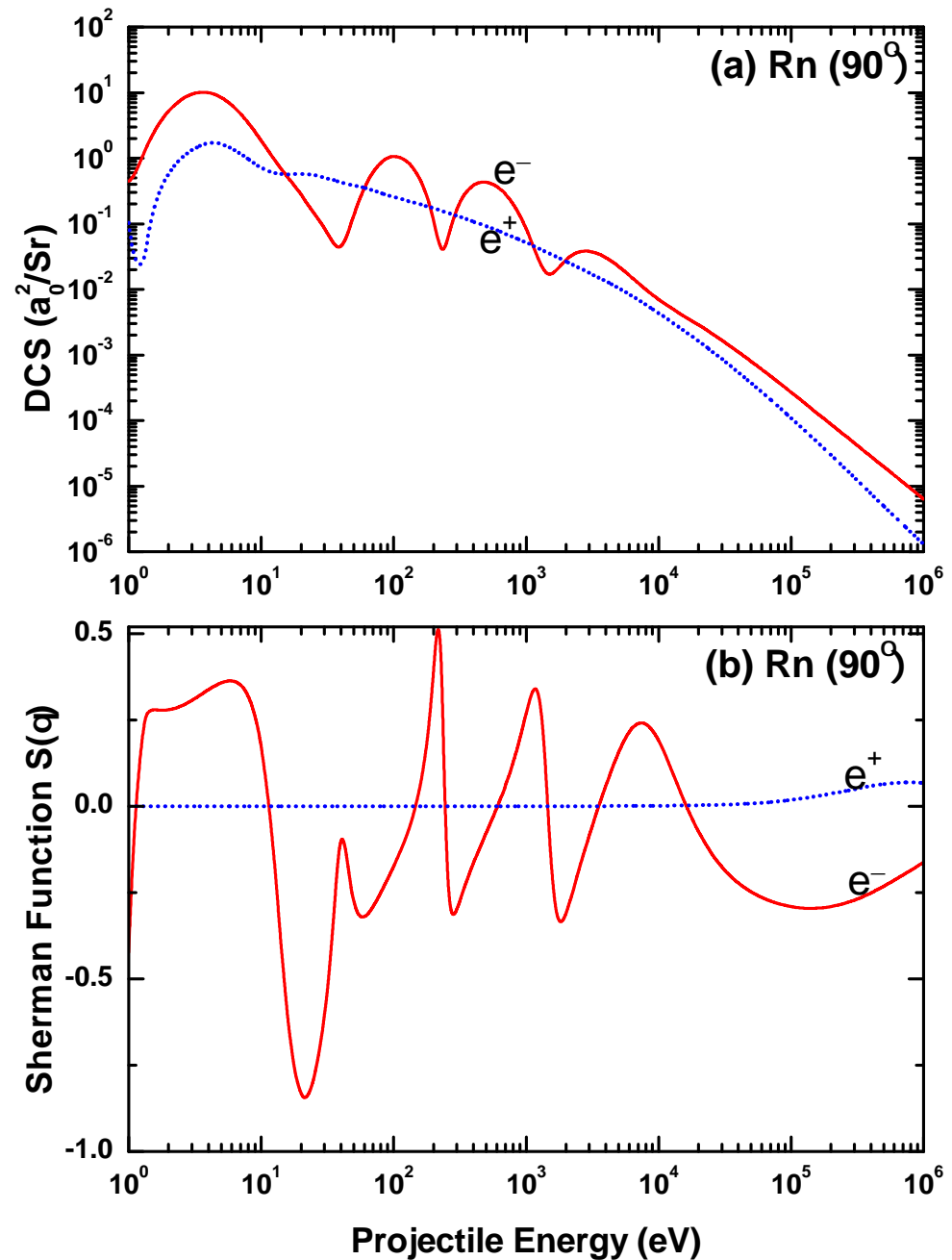
**Figure 31.** Angular variation of the scaled differential cross section for  $e^{-}\text{-Rn}^{q+}$  scattering at different energies for the ionicities  $q =$  (a) 40, (b) 55 and (c) 70. Furthermore, are present the scaled Rutherford cross sections for the same scattering systems.

Figure 31 also revealed that, for a particular ion charge, the width of the maximum increases with increasing energy, the ratio of ion DCS to Rutherford DCS decreases with the increase of ion charge. One can also observed that, with the increase of ion charge, the strongest Coulomb glory shifts toward low incident energy. This is expected because the strength of the potential of the electronic cloud at the origin is stronger for lower degree of ionicities than higher ones. It means that ion-target of high ion charge can cause low energy electron to get backscattered and vice versa. This causes strongest Coulomb glory to be observed at low incident energy for higher ion charge and at comparatively high incident energy for low ion charge.

#### 4.4. Comparison of the Electron and Positron Impact Results

In Figure 32, we compare the energy dependent DCS and the corresponding Sherman function results at  $90^\circ$  for the scattering of electrons and positrons from neutral radon atoms. The basic features of the DCS in the energy region above some tens of eV up to a few keV are oscillations originated due to the diffraction of the projectile beam by the atomic target electrons. The structures disappear when the collision becomes energetic enough so that the beam has passed even the innermost K-shell electrons before the scattering events take place. As seen in Figure 32a, for electron impact scattering, three DCS minima appear within  $E_i = 30$  eV to 3 keV, and beyond that the DCS decreases monotonously with increasing energy. For positron impact scattering, on the other hand, the number of DCS minima reduces to 2 and confined to low energies: the first minimum is at 2 eV and the second one at 20 eV. The reduced number of DCS minima for positron projectile is due to the absence of exchange potential, and low energy structure is the influence of the correlation polarization potential. One can also see from Figure 32a that the values of positron DCS at all energies are smaller than those of electron DCS. This feature supports the fact that the target electrons do not serve as scattering centers for the positrons. Instead, they screen the central field, thereby lowering the DCS as compared to its electron counterpart.

Figure 32b displays the Sherman function results comparing between the electron and positron impact scattering. For the case of electron scattering, pronounced structures are observed in the Sherman function, the positions of which strongly correlate to those in the DCS. For positron projectile, on the other hand, no structure appears up to 100 keV, and the value of spin asymmetry is extremely low. This fact can be related to the repulsive potential which prevents the positron to penetrate the nucleus in contrast to its electron counterpart.



**Figure 32.** Comparison of (a) the differential cross section and (b) the corresponding Sherman function for the collisions of electrons and positrons from neutral radon targets at the scattering angle of  $90^\circ$ .

In Figure 33, we compare our spin polarization parameters  $U$  and  $T$  results, respectively, in Figure 33a,b, between electron and positron impact scatterings at fixed angle  $\theta = 90^\circ$ . It is revealed that, for electron scattering, multiple structures appear in both  $U$  and  $T$  up to several hundred keV. However, the structures are more stronger at lower energy

and become less pronounced with increasing energy. For positron scattering, on the other hand, no structures are observed in  $U$  and  $T$ . Starting from zero the  $U$  parameter increases very slowly with energy up to 300 keV and then increases rapidly. The same feature is also observed in the case of  $T$  parameter but with opposite sign.

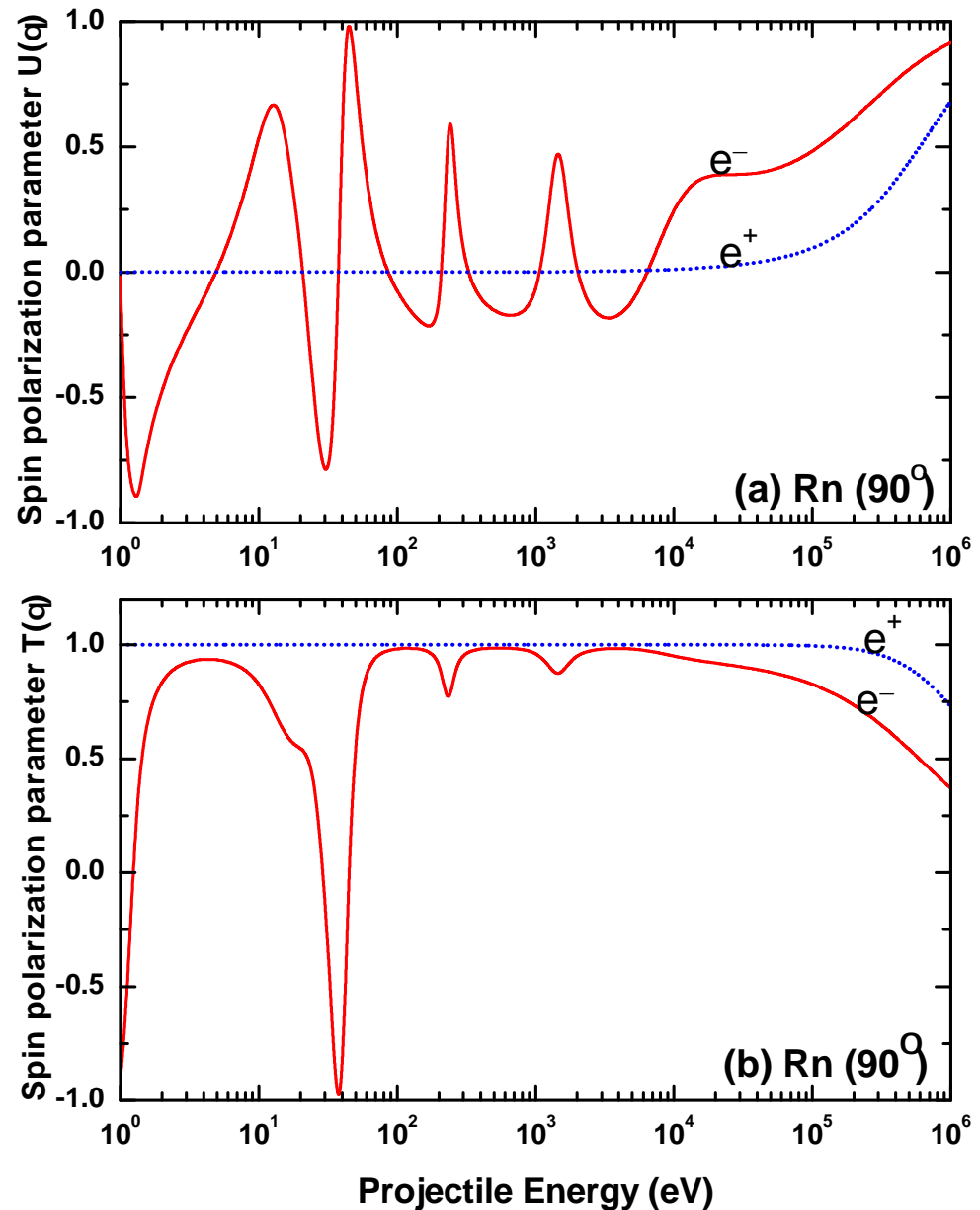
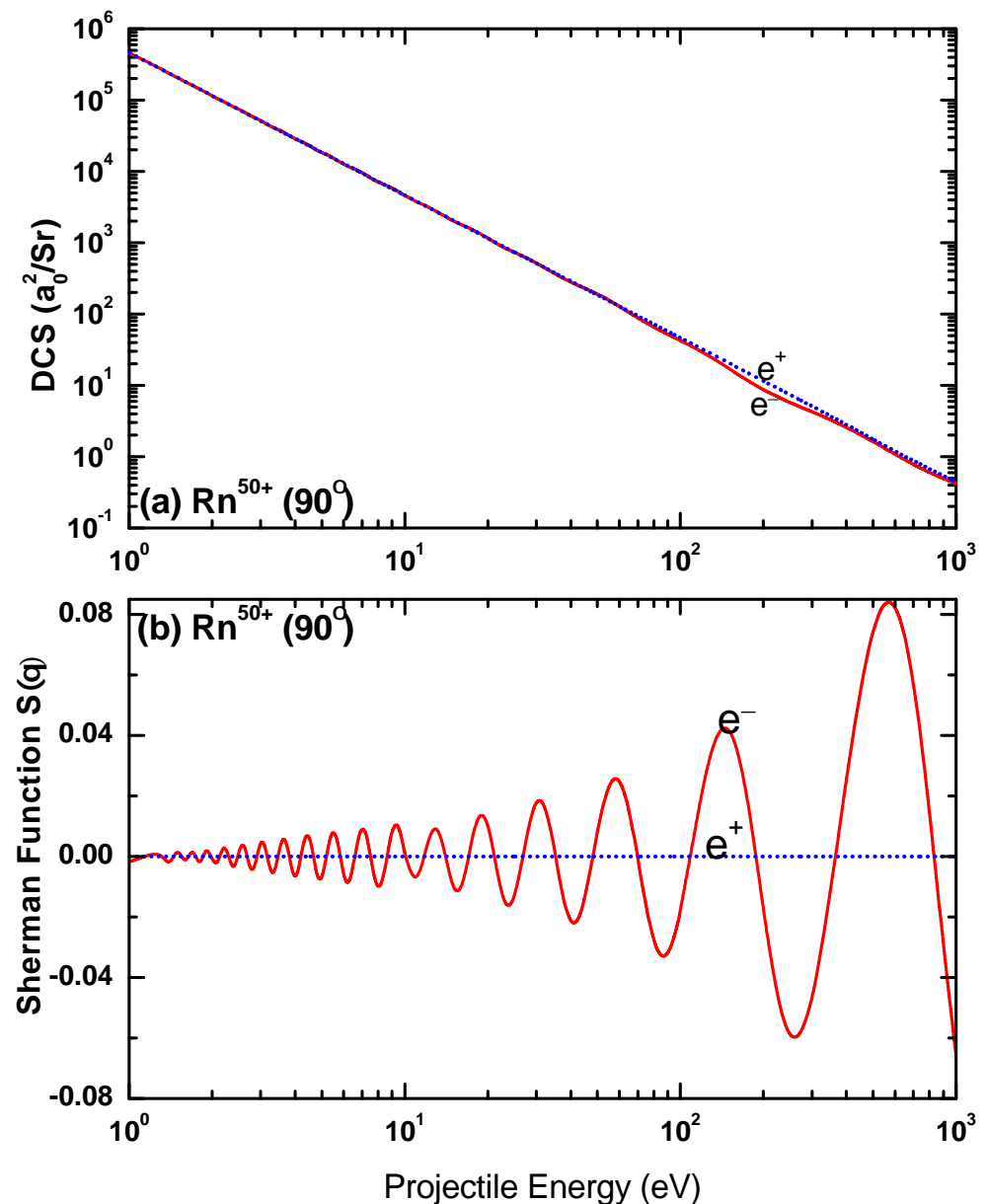


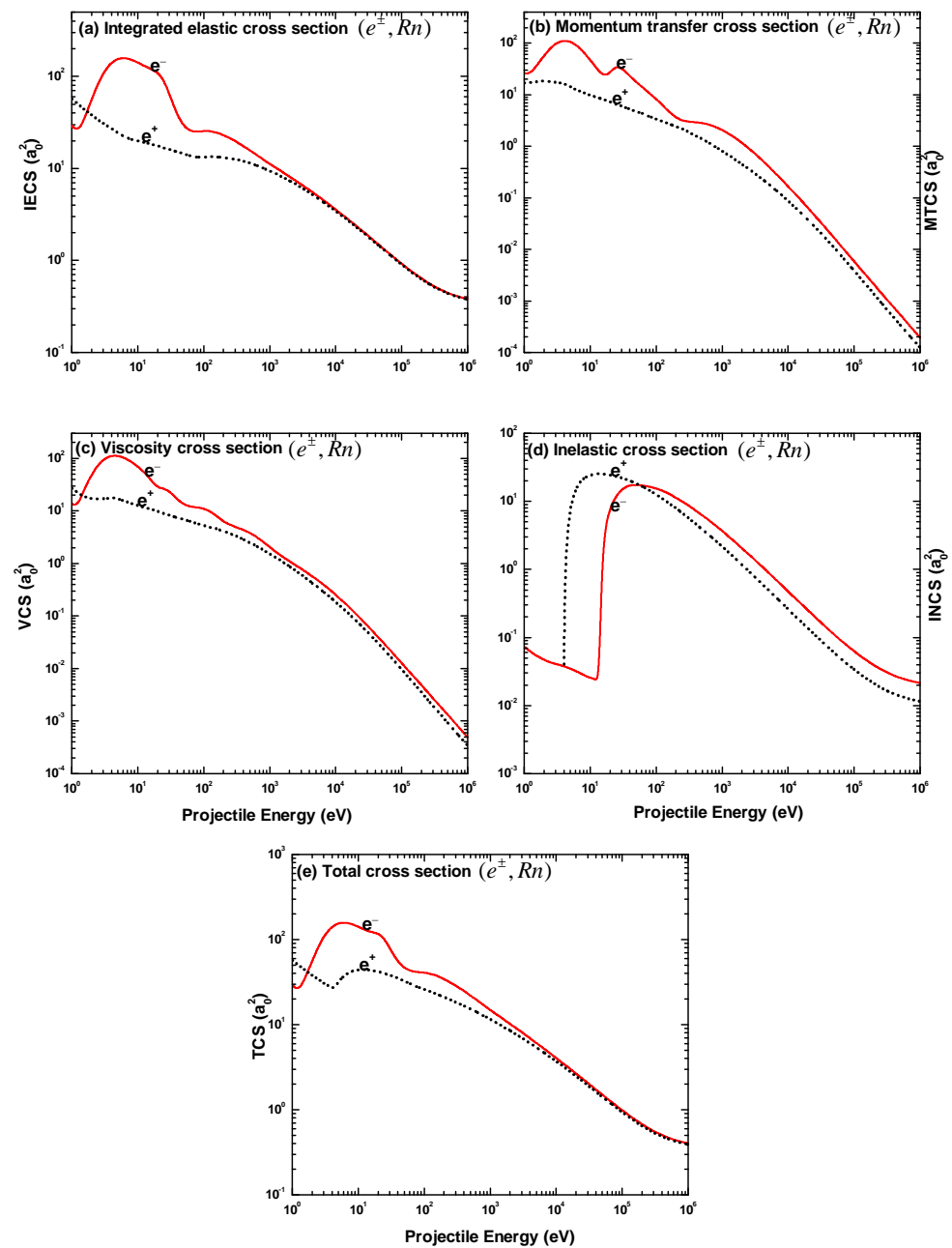
Figure 33. Comparison of (a) the differential cross section and (b) the corresponding Sherman function for the collisions of electrons and positrons from  $\text{Rn}^{50+}$  ion targets at the scattering angle of  $90^\circ$ .

Figure 34 compares the DCS and the Sherman functions of the electron and positron impact scattering from  $\text{Rn}^{50+}$  ion targets. There is no significant difference between electron and positron DCSs except a shallow minimum observed at 200 eV in electron DCS. In electron impact Sherman function shows multiple structures with higher excursion with increasing energy, whereas the Sherman function, for positron impact scattering, is almost zero all through the displayed energy domain.



**Figure 34.** Comparison of (a) the differential cross section and (b) the corresponding Sherman function for the collisions of electrons and positrons from  $\text{Rn}^{50+}$  ion targets at the scattering angle of  $90^\circ$ .

In Figure 35, we depict energy variation of the IECS, MTCS, VCS, INCS and TCS results for electron scattering from neutral radon atoms in comparison with those for positron impact scattering. The comparison shows, at higher energy region (well above 1 keV), no significant difference in the above mentioned observables between the two collision systems. However, at lower energy region ( $E_i < 1$  keV), the cross sections produce a remarkable change with changing the projectile. The R-T structures, for electron projectile, are stronger both in number and intensity than those for positron counterpart. This result indicates that the exchange, the polarization and the absorption potentials almost vanish at energies beyond 1 keV. Furthermore, the static part, opposite in sign for the two projectiles, is the sole contributor to the scattering and the potentials, with the same magnitude but opposite in sign, make the same contribution to the scattering.



**Figure 35.** Comparison of IECS, MTCS, VCS, INCS and TCS results for the collisions of electrons and positrons from neutral radon at the scattering angle of  $90^\circ$ .

### 5. Conclusions

In this paper, we report on the calculations of DCS, IECS, MTCS, VCS, INCS, TCS and spin asymmetry parameters  $S$ ,  $U$  and  $T$  for both the electrons and positrons impact scattering from radon isonuclear series over a wide collision energy  $1 \text{ eV} \leq E_i \leq 1 \text{ MeV}$ . The aforesaid scattering observables have been calculated within Dirac relativistic partial wave analysis employing a modified Coulomb potential. For the first time, the present study furnishes the detailed analysis of the CM in the DCS distributions and the total spin-polarization in the elastic scattering of electrons from neutral radon atoms. We also present SDCS and RDCS, and demonstrate the Coulomb glory effects. We have not found any experimental results, available in the literature, of these scattering observables for these scattering systems. However, a comparison of our evaluated cross sections shows a reasonable agreement with the available theoretical results.



As expected, in the low energy DCSs, the present study observes interference structures for electron scattering and structureless behavior in the case of positron scattering, whereas high energy DCSs for these two projectiles are similar in pattern. This indicates that the exchange potential, present in  $e^-$ -atom interaction, is responsible for the production of maxima-minima. The same effect causes greater number of maxima-minima in the angular distributions of DCS and  $S$ , at different energies, for the former scattering system than the latter. Furthermore, this effect is negligible at high energies, thereby leading to the almost parallel behavior of the DCS for both the projectiles. This study also reveals the effect of the short-range potential, originating from the screening bound electrons, on the cross section up to to charge state  $Rn^{30+}$ . Beyond this charge state, the cross section is almost independent of the charge state, due to the dominance of nuclear potential and diminution of screening effect. The energy dependence of the IECS, MTCS, VCS, INCS and TCS shows a non-monotonous pattern of the minimum-maximum type up to the collision energy of 1 keV. At all energies and for both the aforesaid projectiles, the DCS maximum occurs at the scattering angle  $\theta = 0$  and it gradually falls off with the increase of the scattering angle in region of small angles. This arises due to the property of the Legendre polynomial factor in the expression for  $f(\theta)$  in the Equation (30).

For the present electron impact scattering, we obtain 18 deep DCS minima including 14 CMs, where the DCS attains its smallest value. In the proximity of these CMs, we determine 28 MSP points where the spin polarization varies from +0.92 to +1.00 and from  $-0.84$  to  $-1.00$ , respectively, in positive and negative excursions. All of these MSP points can be termed as the total polarization points. These results demonstrate the efficacy of the present modified Coulomb potential in determining accurately the deepest DCS valley and CM positions. Pronounced Coulomb glory effect, an amplification of elastic backscattering due to the attractive screened Coulomb potential, is observed in the angular distribution of elastically scattered electrons. Because of the strength of the potential of electronic cloud to scatter electron through  $\theta = 180^\circ$ , the strongest Coulomb glory effect is seen to shift towards lower charge state. All of these analyses for  $e^\pm$ -Rn scattering systems still await verification by future experimental as well as theoretical studies.

**Author Contributions:** M.H.K.: investigation, writing and review; A.K.F.H.: methodology and supervision; M.M.H.: writing original draft preparation and Editing; M.M.B.: data curation and editing. H.W.: review and resources; M.A.U.: software, review and conceptualization. All authors have read and agreed to the published version of the manuscript.

**Funding:** This research received no external funding.

**Conflicts of Interest:** The authors declare no conflict of interest.

## References

- Andersen, N.; Gallagher, J.W.; Hertel, I.V. Collisional alignment and orientation of atomic outer shells I. Direct excitation by electron and atom impact. *Phys. Rep.* **1988**, *165*, 1–188. [\[CrossRef\]](#)
- Müller, A. Fundamentals of electron-ion interaction. *Hyperfine Interact.* **1996**, *99*, 31–45. [\[CrossRef\]](#)
- Jean, P.; Gillard, W.; Marcowith, A.; Ferrière, K. Positron transport in the interstellar medium. *Astron. Astrophys.* **2009**, *508*, 1099–1116. [\[CrossRef\]](#)
- Massey, H.S.W., Lawson, J. Thompson, D.G. Quantum theory of atoms, molecules and the solid state. In *A tribute to John C. Slater*; Academic Press: New York, NY, USA, 1966.
- Tioukine, V.; Aulenbacher, K.; Riehn, E. A Mott polarimeter operating at MeV electron beam energies. *Rev. Sci. Instr.* **2011**, *82*, 033303. [\[CrossRef\]](#)
- Afroz, S.; Haque, M.M.; Haque, A.F.; Jakubassa-Amundsen, D.H.; Patoary, M.A.R.; Shorifuddoza, M.; Khandker, M.H.; Uddin, M.A. Elastic scattering of electrons and positrons from  $^{115}\text{In}$  atoms over the energy range 1 eV–0.5 GeV. *Results Phys.* **2020**, *18*, 103179. [\[CrossRef\]](#)
- Hassan, R.; Haque, M.M.; Haque, A.K.F.; Shorifuddoza, M.; Khandker, M.H.; Patoary, M.A.R.; Basak, A.K.; Maaza, M.; Saha, B.C.; Uddin, M.A. Relativistic study on the scattering of electrons and positrons from atomic iron at energies 1 eV–10 keV. *Mol. Phys.* **2020**, *119*, 1849838. [\[CrossRef\]](#)
- McKenna, P.; Williams, I.D. Differential cross section measurements for elastic scattering of electrons from  $\text{Ar}^{2+}$  and  $\text{Xe}^{2+}$ . *Phys. Scr.* **2001**, *T92*, 370–372. [\[CrossRef\]](#)

9. Brotton, S.J.; McKenna, P.; Gribakin, G.; Williams, I.D. Angular distribution for the elastic scattering of electrons from  $\text{Ar}^+(3s^23p^52P)$  above the first inelastic threshold. *Phys. Rev. A* **2002**, *66*, 062706. [[CrossRef](#)]
10. Kauppila, W.E.; Kwan, C.K.; Przybyla, D.; Smith, S.J.; Stein, T.S. Positron–inert-gas-atom elastic DCS measurements. *Can. J. Phys.* **1996**, *74*, 474–482. [[CrossRef](#)]
11. Gulley, R.J.; Alle, D.T.; Brennan, M.J.; Brunger, M.J.; Buckman, S.J. Differential and total electron scattering from neon at low incident energies. *J. Phys. B* **1994**, *27*, 2593. [[CrossRef](#)]
12. Baluja, K.L.; Jain, A. Positron scattering from rare gases (He, Ne, Ar, Kr, Xe, and Rn): Total cross sections at intermediate and high energies. *Phys. Rev. A* **1992**, *46*, 1279. [[CrossRef](#)]
13. Lam, L.S.F. Relativistic effects in electron scattering by atoms. III. Elastic scattering by krypton, xenon and radon. *J. Phys. B At. Mol. Phys.* **1982**, *15*, 119. [[CrossRef](#)]
14. Khandker, M.H.; Billah, M.M.; Watabe, H.; Haque, A.K.F.; Uddin, M.A. Theoretical studies on the elastic scattering of  $e^\pm$  off the ions of xenon isonuclear series. *Phys. Scr.* **2020**, *96*, 025402. [[CrossRef](#)]
15. Khandker, M.H.; Haque, A.K.F.; Maaza, M.; Uddin, M.A. Scattering of  $e^\pm$  from the neon isonuclear series over the energy range 1 eV–0.5 GeV. *Jap. J. Appl. Phys.* **2020**, *59*, SHHA05. [[CrossRef](#)]
16. Khandker, M.H.; Haque, A.K.F.; Maaza, M.; Uddin, M.A. Elastic scattering of electrons from the ions of argon isonuclear series. *Phys. Scr.* **2019**, *94*, 075402. [[CrossRef](#)]
17. Haque, M.M.; Haque, A.K.F.; Jakubassa-Amundsen, D.H.; Patoary, M.A.R.; Basak, A.K.; Maaza, M.; Saha, B.C.; Uddin, M.A.  $e^\pm$  Ar scattering in the energy range  $1 \text{ eV} \leq E_i \leq 0.5 \text{ GeV}$ . *J. Phys. Commun.* **2019**, *3*, 045011. [[CrossRef](#)]
18. Kapil, K.S.; Vats, R.P. Elastic positron scattering by radon and radium atoms. *Phys. Scr.* **2012**, *85*, 045304. [[CrossRef](#)]
19. Tripathi, A.N.; Jain, A.K. Spin polarization and cross sections in elastic scattering of electrons from Yb, Rn, and Ra atoms. *Phys. Rev. A* **2000**, *61*, 032713.
20. Mayol, R.; Salvat, F. Total and transport cross sections for elastic scattering of electrons by atoms. *At. Data Nucl. Data Tables* **1997**, *65*, 55–154. [[CrossRef](#)]
21. Dapor, M.; Miotello, A. Differential, total, and transport cross sections for elastic scattering of low energy positrons by neutral atoms ( $Z=1-92$ ,  $E=500-4000 \text{ eV}$ ). *At. Data Nucl. Data Tables* **1998**, *69*, 1–100. [[CrossRef](#)]
22. Haque, M.M.; Haque, A.K.F.; Bhattacharjee, P.P.; Uddin, M.A.; Patoary, M.A.R.; Basak, A.K.; Maaza, M.; Saha, B.C. Relativistic treatment of scattering of electrons and positrons by mercury atoms. *Mol. Phys.* **2019**, *117*, 2303–2319. [[CrossRef](#)]
23. Haque, A.K.F.; Haque, M.M.; Bhattacharjee, P.P.; Uddin, M.A.; Patoary, M.A.R.; Hossain, M.I.; Basak, A.K.; Mahbub, M.S.; Maaza, M.; Saha, B.C. Relativistic calculations for spin-polarization of elastic electron–mercury scattering. *J. Phys. Commun.* **2017**, *1*, 035014. [[CrossRef](#)]
24. Hassan, R.; Abdullah, M.N.A.; Shorifuddoza, M.; Khandker, M.H.; Patoary, M.A.R.; Haque, M.M.; Das, P.K.; Maaza, M.; Billah, M.M.; Haque, A.K.F.; Uddin, M.A. Scattering of  $e^\pm$  off silver atom over the energy range 1 eV–1 MeV. *Eur. Phys. J. D* **2021**, *75*, 1–23. [[CrossRef](#)]
25. Kumar, A.; Abdullah, M.N.A.; Haque, A.K.F.; Singh, I.; Uddin, M.A. Elastic scattering of electrons by Sr atom: a study of critical minima and spin polarization. *J. Phys. Commun.* **2019**, *3*, 065001. [[CrossRef](#)]
26. Desclaux, J. P. A multiconfiguration relativistic Dirac-Fock program. *Comp. Phys. Commun.* **1975**, *9*, 31–45. [[CrossRef](#)]
27. Hahn, B. Ravenhall, D.G. Hofstadter, R. High-energy electron scattering and the charge distributions of selected nuclei. *Phys. Rev.* **1956**, *101*, 1131. [[CrossRef](#)]
28. Jakubassa-Amundsen, D.H.; Barday, R. The Sherman function in highly relativistic elastic electron–atom scattering. *J. Phys. G Nucl. Part. Phys.* **2012**, *39*, 025102. [[CrossRef](#)]
29. Furness, J.B.; McCarthy, I.E. Semiphenomenological optical model for electron scattering on atoms. *J. Phys. B At. Mol. Phys.* **1973**, *6*, 2280. [[CrossRef](#)]
30. Salvat, F. Optical-model potential for electron and positron elastic scattering by atoms. *Phys. Rev. A* **2003**, *68*, 012708. [[CrossRef](#)]
31. Mittleman, M.H.; Watson, K.M. Effects of the Pauli principle on the scattering of high-energy electrons by atoms. *Ann. Phys.* **1960**, *10*, 268. [[CrossRef](#)]
32. Perdew, J.P.; Zunger, A. Self-interaction correction to density-functional approximations for many-electron systems. *Phys. Rev. B* **1981**, *23*, 5048. [[CrossRef](#)]
33. Jain, A. Low-energy positron-argon collisions by using parameter-free positron correlation polarization potentials. *Phys. Rev. A* **1990**, *41*, 2437. [[CrossRef](#)]
34. Salvat, F.; Jablonski, A.; Powell, C.J. ELSEPA—Dirac partial-wave calculation of elastic scattering of electrons and positrons by atoms, positive ions and molecules. *Comput. Phys. Commun.* **2005**, *165*, 157–190. [[CrossRef](#)]
35. Rose, M.E. *Relativistic Electron Theory*; Wiley: New York, NY, USA, 1961.
36. Salvat, F.; Fernandez-Varea, J.M.; Williamson, W. Accurate numerical solution of the radial Schrödinger and Dirac wave equations. *Comput. Phys. Commun.* **1995**, *90*, 151. [[CrossRef](#)]
37. Kessler, J. Electron spin polarization by low-energy scattering from unpolarized targets. *Rev. Mod. Phys.* **1969**, *41*, 3. [[CrossRef](#)]
38. Maiorova, A.V.; Telnov, D.A.; Shabaev, V. M.; Tupitsyn, I.I.; Plunien, G.; Stöhlker, T. Backward scattering of low-energy antiprotons by highly charged and neutral uranium: Coulomb glory. *Phys. Rev. A* **2007**, *76*, 032709 [[CrossRef](#)]
39. Lucas, M.W.; Jakubassa-Amundsen, D.H.; Kuzel, M.; Groeneveld, K.O. Quasifree electron scattering in atomic collisions: The Ramsauer–Townsend effect revisited. *Int. J. Mod. Phys. A* **1997**, *12*, 305–78. [[CrossRef](#)]

- 
40. Carlsson, T.A. *Photoelectron and Auger Spectroscopy*; Springer Science & Business Media: New York, NY, USA, 1975
  41. Walker, D.W. Relativistic effects in low energy electron scattering from atoms. *Adv. Phys.* **1971**, *20*, 257–323. [[CrossRef](#)]
  42. Haque, A.K.F.; Uddin, M.A.; Jakubassa-Amundsen, D.H.; Saha, B.C. Comparative study of eV to GeV electrons and positrons scattering elastically from neutral atoms. *J. Phys. B* **2018**, *51*, 175202. [[CrossRef](#)]